# ABSTRACT

Title of dissertation: ROOM TEMPERATURE LIGHT-MATTER INTERACTION USING QUANTUM DOTS AND PHOTONIC CRYSTAL CAVITIES

Shilpi Gupta, Doctor of Philosophy, 2014

Dissertation directed by: Professor Edo Waks
Department of Electrical and Computer Engineering

Control over spontaneous emission is important for many applications in photonics, including efficient light-emitting diodes, photovoltaics, single-photon sources and low-threshold nanolasers. Photonic crystals can modify the spontaneous emission by creating cavities with extremely small mode-volumes, and are an ideal platform for integrated devices because of their scalable planar architecture. For developing photonic devices at room temperature using such cavities, colloidally synthesized quantum dots are excellent emitters because they exhibit high photoluminescence efficiency and emission wavelength tunability.

In this thesis, I present experimental and theoretical work on enhancing light-matter interaction at room temperature, using colloidal quantum dots and nanobeam photonic crystal cavities. Using time-resolved optical spectroscopy, we observed enhanced spontaneous emission rate of the quantum dots coupled to the cavity mode. We also demonstrated saturable absorption of the quantum dots coupled to the cavity mode by pump-intensity dependent cavity-linewidth, which is a nonlinear

phenomenon with potential applications in optical switching at room temperature. Using the quantum optics framework, we developed a theoretical model to show that cavity-enhanced spontaneous emission can be used to overcome Auger recombination (an ultrafast nonradiative process that quenches optical gain) in colloidal quantum dots to develop low-threshold nanolasers. In the end, I will also discuss our current efforts towards deterministic deposition of quantum dots on photonic crystal cavities using atomic force microscopy for effective fabrication of quantum dot devices.

# ROOM TEMPERATURE LIGHT-MATTER INTERACTION USING QUANTUM DOTS AND PHOTONIC CRYSTAL CAVITIES

by

Shilpi Gupta

Dissertation submitted to the Faculty of the Graduate School of the
University of Maryland, College Park in partial fulfillment
of the requirements for the degree of
Doctor of Philosophy
2014

Advisory Committee:
Professor Edo Waks, Chair/Advisor
Professor Thomas E. Murphy
Professor Christopher C. Davis
Professor Jeremy N. Munday
Professor Steven L. Rolston

# Dedication

I dedicate this thesis to my parents.

# Acknowledgments

First, I thank my advisor, Professor Edo Waks for his support and guidance throughout my PhD work. I learnt from him the importance of asking questions, and finding answers systematically. His enthusiasm for science kept me going when things were not working well in the lab. I look up to him for both his scientific acumen and professional attitude with which he leads the group.

I would like to thank Professor Thomas Murphy, Professor Christopher Davis, Professor Jeremy Munday and Professor Steven Rolston for being on my thesis committee and for their continuous guidance. I have collaborated with Professor Davis and Professor Munday's lab, and I am thankful to them for their support. I am grateful to my undergraduate research advisors, Professor M. R. Shenoy and Professor K. Thyagarajan for introducing me to the field of optics and for their continuous encouragement till today.

I am fortunate to be a part of a warm and close-knit research group. I thank all my labmates: Deepak Sridharan, Chad Ropp, Ranojoy Bose, Kangmook Lim, Thomas Shen, Hyochul Kim, Shuo Sun, Tao Cai and Kaushik Roy for their support and help. Special thanks to Chad for mentoring me on optical measurement techniques and for always taking out time to help me in lab. Towards the end of my PhD, I collaborated with Joseph Garrett for dip-pen nanolithography project, and it has been a pleasure working with him. He is an AFM expert and always has innovative ideas to solve problems.

Fabrication has been a major part of my work, and it would not have been

possible without the continuous support from the UMD nanocenter staff: Tom Loughran, Jon Hummel, John Abrahams, and Larry Lai. I thank them all for taking excellent care of the tools and always being there to help. I also thank Mario Urdaneta for letting me use his glove box, without which my quantum dots would not have survived for very long.

I acknowledge support from IREAP staff members. I thank Jay Pyle for machining help, Ed Condon for IT support, Nancy Boone for purchasing help, and Dorothea Brosius for taking care of all of us. I would also like to thank staff members at ECE graduate office: Dr. Tracy Chung, Melanie Prange, Vivian Lu and Maria Hoo for their kind support.

In my initial years at College Park, I was lucky to have found friends who have stood by me since then. I thank Neeraja, Prasad, Joe and Soumya for the wonderful company. I would also like to acknowledge my friends from high-school and college Neha, Parijat, and Jyothi for their unwavering support and affection.

I owe my deepest thanks to my father and my mother for their unconditional love and support. I am grateful to them for giving me freedom to pursue what I enjoyed, and standing by me at every step whether I failed or succeeded. My brother has been my stress-buster all these years, and I thank him for patiently listening to me. And finally, I thank my husband who has been my pillar of strength. He has pulled me out of the deep lows that I frequently fell into, and has instilled confidence in me time and again. His love for his locusts has inspired me to remain affectionate towards my quantum dots.

# Table of Contents

# List of Tables



# List of Figures

# Chapter 1: Introduction

## 1.1 Motivation

Control over spontaneous emission is important for many applications in nanophotonics, including fast and low-threshold nanolasers [1–4] for optical communication and computing, efficient light-emitting diodes [5] for displays and lighting, efficient photovoltaics [6, 7] for solar power harvesting, and efficient single-photon sources [8, 9] for quantum information processing. Spontaneous emission can be controlled (enhanced or inhibited) by modifying the properties of the radiation field — photonic density of states and the electric-field strength at the emitter's location [10] — using optical cavities. Photonic crystals are an ideal platform for nanophotonic devices because of their scalable planar architecture and extremely small mode-volume cavities. Moreover, the interaction of quantum dots with a cavity can lead to enhanced nonlinear optical effects such as optical bistability [11–14] and saturable absorption [15–17], which can enable all-optical signal processing devices [18–20].

In this thesis, I present experimental and theoretical work towards enhancing light-matter interaction at room temperature, using colloidal quantum dots and photonic crystal cavities. In this chapter, I will introduce photonic crystal cavities and colloidal quantum dots.

## 1.2 Photonic crystal cavities

Photonic crystals are formed by periodic variation of refractive index in an optical medium. The control of light in photonic crystals happens via distributed Bragg reflection that leads to formation of photonic band gaps analogous to the electronic bandgaps in semiconductors. The propagation of light at frequencies within the photonic bandgap is prohibited along certain directions. The most common forms of photonic crystals are 2D and 1D (fig. 1.1 shows photonic crystals in SiN, fabrication is described in Chapter 2), in which light propagation is governed by distributed Bragg reflection in two and one dimensions respectively, and by total internal reflection in the rest of the directions. Typically, these photonic crystals are fabricated by patterning a periodic lattice of holes in a thin, suspended membrane of high refractive index material. Both 2D and 1D photonic crystals can be fabricated using the standard techniques employed in the semiconductor industry.

Light can be confined by creating defects, known as photonic crystal cavities, in the periodicity of the photonic crystals. These cavities can be formed by locally missing, shrinking or shifting the holes (fig. 1.2 shows photonic crystal cavities in SiN, fabrication is described in Chapter 2). In this work, I have used 1D (nanobeam) photonic crystal cavities, which confine light in SiN. The mode-profile of the nanobeam photonic crystal cavity is shown in fig. 1.3. Nanobeam photonic crystal cavities have been previously studied in a variety of material systems, such as silicon [21–23], silicon nitride [24, 25], silicon dioxide [26–28], and gallium arsenide [29, 30], and have been theoretically predicted to achieve mode-volumes

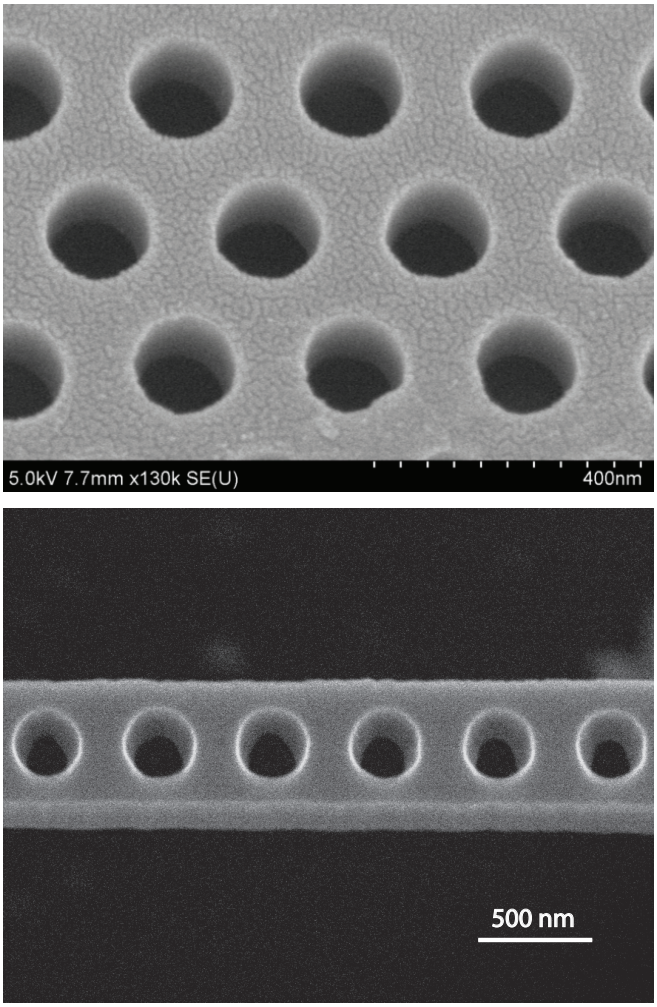


Figure 1.1: SEM image of (a) a 2D photonic crystal , (b) a 1D (nanobeam) photonic crystal in SiN.

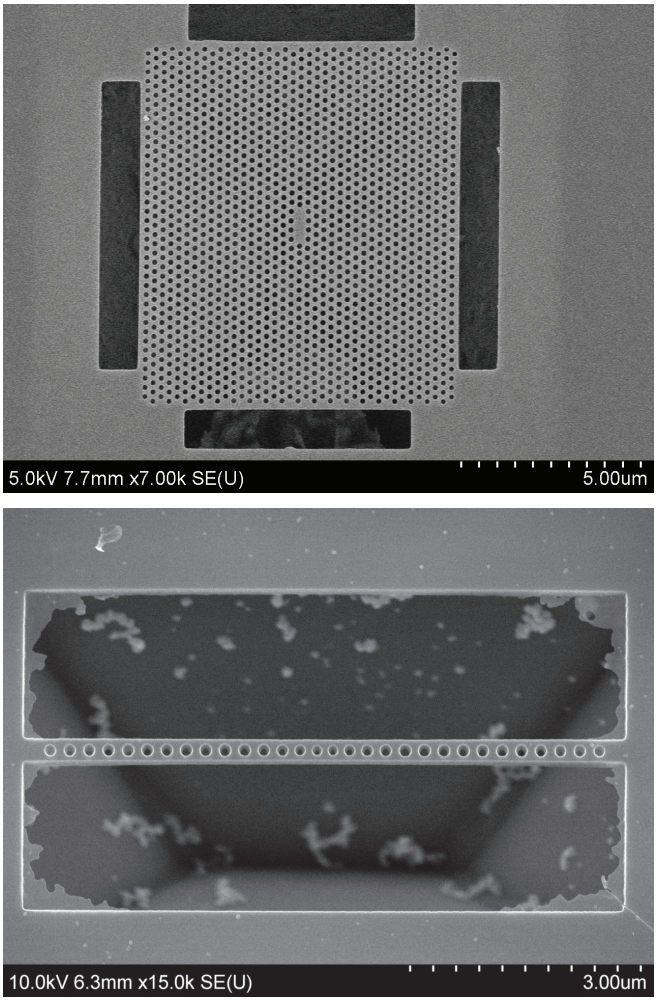


Figure 1.2: SEM image of a typically fabricated (a) 2D photonic crystal cavity, (b) 1D (nanobeam) photonic crystal cavity in SiN.

approaching the diffraction limit [22,23,28,31]. We utilize a cavity design proposed by Khan et al. [25] for our experiments. The fabrication details are explained in Chapter 2.

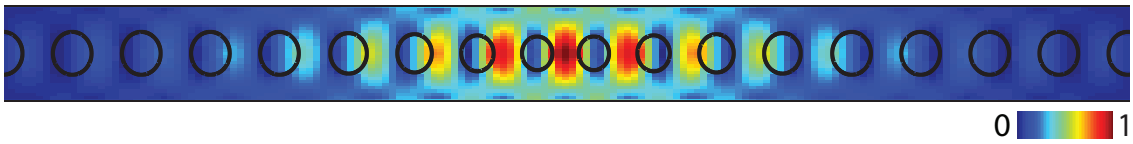


Figure 1.3: The simulated mode-profile of the nanobeam photonic crystal cavity in SiN.

## 1.3 Quantum dots

Quantum dots are semiconductor nanocrystals which exhibit discrete energy levels due to three-dimensional confinement of the charge carriers. Because of these discrete energy levels, quantum dots behave much like atoms. The emission properties of the quantum dots are determined by their shape, size and material composition.

There are two types of quantum dots: epitaxial quantum dots and colloidal quantum dots. Epitaxial quantum dots are three dimensional islands of a lower bandgap semiconductor, self-assembled in a high bandgap host semiconductor. These are grown by a molecular beam epitaxy technique. Colloidal quantum dots are synthesized in solution form [32]. These quantum dots are not restricted to any host material, and therefore, can be incorporated with any photonic device.

CdSe quantum dots are among the most mature colloidal quantum dots. These

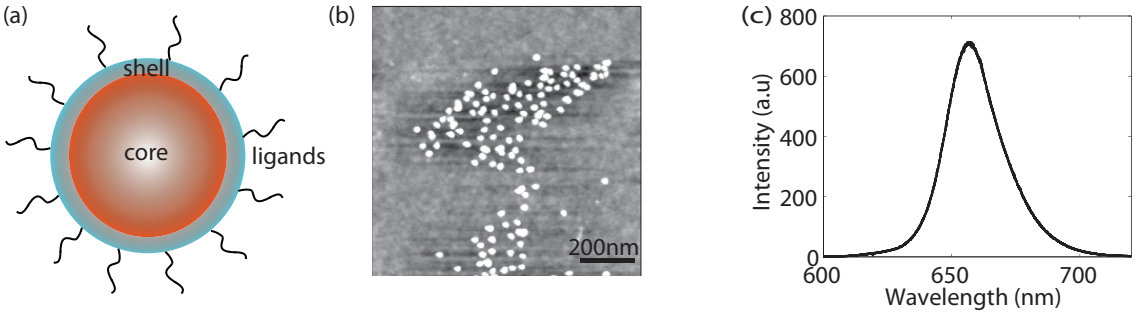


Figure 1.4: (a) Schematic of a colloidal quantum dot, comprising of a core, a shell and ligands. (b) An AFM image of CdSe/ZnS quantum dots dried on a SiN surface. (c) A typical photoluminescence spectrum of a an ensemble of CdSe/ZnS quantum dots at room temperature.

quantum dots comprise of three main sections: a core, a shell and a coating of ligands, as shown schematically in fig. 1.4(a). The core is a CdSe nanocrystal, the bandgap of which along with the size-dependent confinement of charge carriers determines the band-edge emission wavelength. The shell is comprised of a wider bandgap material such as ZnS or CdS which prevents quenching of the emission due to surface traps. Finally, ligands help in dispersing quantum dots in the desired solvents (water and organic solvents) and in adding functionality to attach them to specific systems. The emission wavelength of CdSe quantum dots can be varied across the entire visible wavelength by manipulating their size during the chemical synthesis [33, 34]. Figure 1.4(b) shows a typical atomic force microscope image of CdSe/ZnS (Invitrogen Qtracker CdSe/ZnS 655 nm) quantum dots dried on a SiN surface and fig. 1.4(c) shows a typical photoluminescence spectrum of an ensemble of CdSe/ZnS quantum dots at room temperature.

## 1.4 Outline of the Thesis

In this thesis, I present both experimental and theoretical work on enhancing interaction between cadmium selenide (CdSe) quantum dots and photonic crystal cavities at room-temperature. Chapter 2 describes the procedure for fabrication of photonic crystal cavities. Chapter 3 describes the time-resolved lifetime measurements on quantum dots located on the photonic crystal cavity, and observation of spontaneous emission enhancement. Chapter 4 describes the experiment demonstrating saturable absorption of quantum dots coupled to the photonic crystal cavity. Chapter 5 discusses a theoretical model for a low-threshold colloidal quantum dot nanolaser. Chapter 6 describes the use of the dip-pen nanolithography technique for deterministic placement of quantum dots on photonic crystal devices. This technique could help in the experimental realization of the proposed nanolaser.

# Chapter 2: Photonic Crystal Cavity Fabrication

## 2.1 Introduction

As described in Chapter 1, photonic crystals can create extremely small mode-volume cavities [35], making them ideal for low-power, on-chip optoelectronic devices [1–4, 19, 36–44] as well as for studying fundamental light-matter interactions. We used nanobeam photonic crystal cavities for our experiments with colloidal quantum dots. This chapter describes the fabrication procedure of these cavities.

## 2.2 Fabrication

We fabricated the devices on 200-nm-thick stoichiometric SiN deposited on silicon using low pressure chemical vapor deposition. We patterned the nanobeam photonic crystal cavities using electron-beam lithography and fluorine-based inductively coupled plasma dry etching. The underlying silicon was etched by aqueous KOH to create a suspended beam. The details of each fabrication step are described below and a schematic of the entire process is shown in Fig. 2.1.

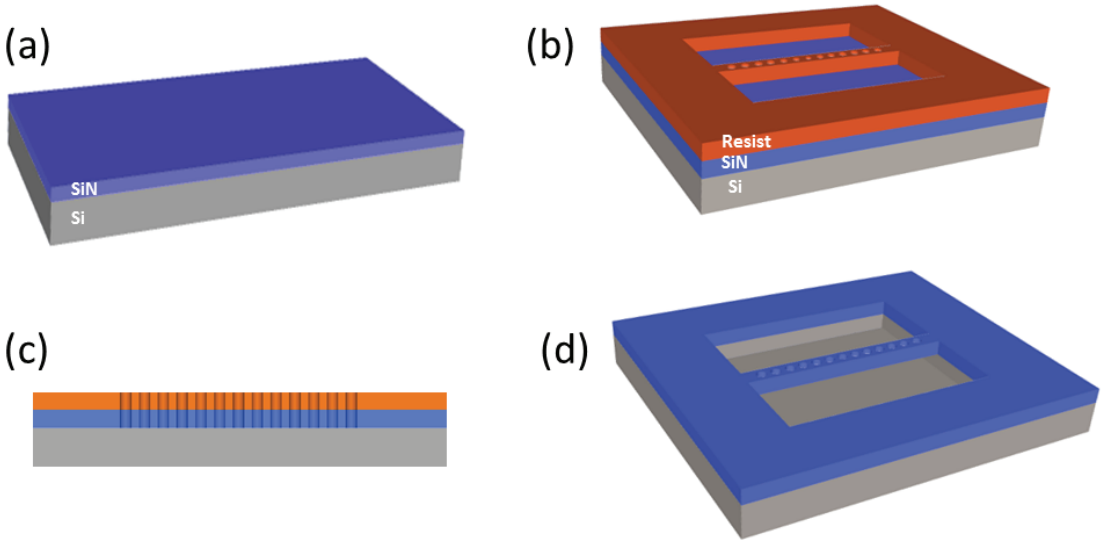


Figure 2.1: Schematic of the fabrication process: (a) deposition of 200 nm SiN on silicon using low pressure chemical vapor deposition (LPCVD), (b) nanobeam PC cavity patterned using e-beam lithography, (c) transfer of the pattern into SiN using inductively coupled plasma etching, and (d) wet etch to to remove the underlying silicon

### 2.2.1 Electron-beam Lithography

Prior to spinning the e-beam resist, the SiN samples were cleaned with acetone, methanol and iso-propanol, and baked on a hotplate at 180 °C for 2 minutes. ZEP520A (Zeon Chemicals), a positive tone e-beam resist, was spun on the samples at 2600 rpm for 1 minute. The sample was again baked at 180 °C for 2 minutes and the resulting resist layer was about 400 nm thick. Because SiN has very low conductivity, it suffers from a charging problem during e-beam writing. To prevent this problem, a conductive polymer layer (aquaSAVE) is spun on the baked resist at 3000 rpm for 1 minute.

E-beam lithography was done using a Raith e-Line system at 30 keV with 7.5 $\mu$m aperture, which gave current in the range of 12 - 20 pA depending on the tip condition and beam alignment. The working distance was set to 10 mm, the write-field area was set to 100×100 $\mu m^2$ and the step-size for both area and curved elements was set to 4 nm. Since the nanobeam cavity structure includes two patterns (side-rectangles and holes) which differ in area considerably, the two were given different dosages during exposure, and an array of dosages, centered around the optimal value, was used during e-beam exposure. Typical SEM images of a cross-sectional view of the mask of an array of trenches and photonic crystal holes are shown in fig. 2.2.

After e-beam exposure, the samples were developed: first the conducting polymer layer was rinsed off using water and the samples were nitrogen blow-dried, then the samples were dipped in ZED-N50 (Zeon Chemicals) for 50 seconds, followed by

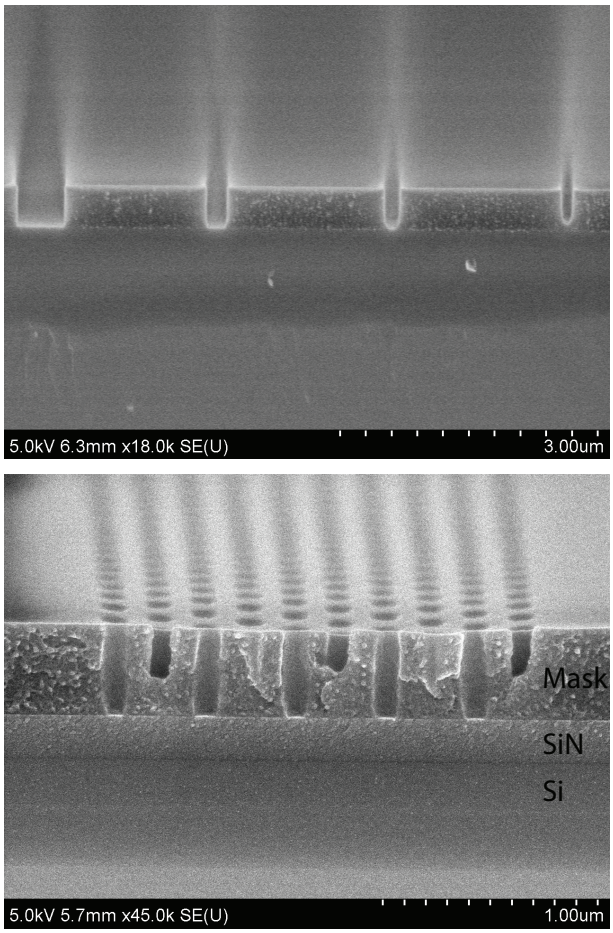


Figure 2.2: SEM image of cross-sectional view of mask of (a) trenches with width 500 nm, 200 nm, 150 nm and 100 nm (b) array of photonic crystal holes of radius 55 nm. The sample is coated with gold for better conductivity.

MIBK (Micro Chem) for 30 seconds, and iso-propanol for 30 seconds.

### 2.2.2 Inductively-coupled Plasma Etching

For transferring the pattern from the mask to SiN, we used inductively-coupled plasma etching (Oxford Plasmalab System 100) under fluorine chemistry. Since the etcher is a shared tool, before etching the samples, it was cleaned by running Oxford's "after SiN-etch" and "after $SiO_2$-etch" clean recipes for 30 minutes each and then by mechanical scrubbing of the chamber from inside using methanol and iso-propanol, which was followed by oxygen plasma run for 30 minutes. The optimized etching recipe (described in Table 2.2.2) was run for 10 minutes to precondition the chamber. A 6" silicon dioxide or silicon nitride wafer was used as a carrier-wafer for the sample. This choice of carrier-wafer ensured optimal values of DC bias. Fomblin pump oil was used to achieve good thermal contact between the sample and the carrier wafer. The optimized etching recipe parameters are listed in Table 2.2.2.

Typical run time was 90 seconds to etch through 200 nm of SiN and about 100 nm of underlying Si, which allowed straighter side-walls. Typical SEM images of cross-sectional view of etched array of trenches and photonic crystal holes are shown in fig. 2.3, where 100 nm of residual resist can also be seen on top. After etching, the residual mask was removed by soaking the sample in Remover PG (Micro Chem) at 80 °C. Most of the times, even after using Remover PG, some residual resist was left near the pattern, which was removed using a mild $O_2$ plasma (Branson Barrel

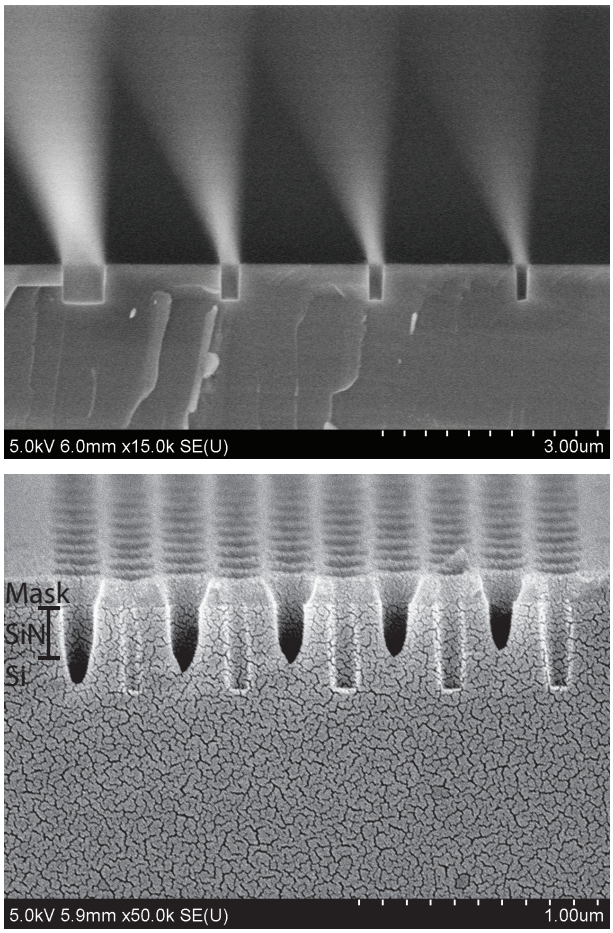


Figure 2.3: SEM image of cross-sectional view of etched (a) trenches with width 500 nm, 200 nm, 150 nm and 100 nm (b) array of photonic crystal holes of radius 55 nm. The sample is coated with gold for better conductivity.

| Parameter | Value |
|---|---|
| $CHF_3$ | 45 sccm |
| $SF_6$ | 5 sccm |
| RF power | 50 W |
| ICP power | 500 W |
| He backing | 7.5 sccm |
| Chamber pressure | 10 mTorr |

Table 2.1: SiN etch recipe parameters.

Resist Stripper; 100 sccm $O_2$, 75W, 2 minutes).

### 2.2.3 Removal of Underlying Silicon

As final step of fabrication, the underlying silicon was etched away to suspend the silicon nitride beams. An aqueous solution of KOH (15 g KOH in 150 mL of DI water) at 80 °C and constantly stirred at 300 rpm was used to undercut the samples. Typical undercut time was 8 minutes. An example SEM image of the final nanobeam structure is shown in fig. 2.4. Similar to e-beam lithography, due to low conductivity of SiN, SEM of SiN structures required carbon coating or gold coating to prevent accumulation of charge on the surface.

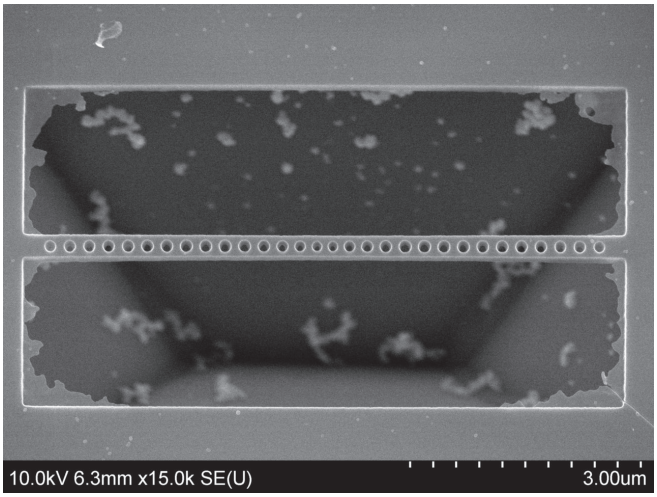


Figure 2.4: SEM image of a typically fabricated nanobeam photonic crystal cavity (reproduced from Fig. 1.2(b)). The sample is coated with carbon for better conductivity.

# Chapter 3: Spontaneous Emission Enhancement

## 3.1 Introduction

Colloidally synthesized quantum dots are excellent emitters for developing light sources [45–49] and non-linear devices [11–13, 15, 18–20] operating at room temperature. These quantum dots exhibit high photoluminescence efficiency at room temperature [50, 51] and emission wavelength tunability [33, 34]. The spontaneous emission rate of the quantum dots can be enhanced by coupling them to small mode-volume cavities [10, 52]. Photonic crystals create extremely small mode-volume cavities [35] that can reduce lasing threshold [1–4, 36–40] and enable nonlinear devices at low light-levels [19, 41–44].

Previous measurements of CdSe quantum dots coupled to photonic crystal cavities have shown increased brightness when the quantum dots are resonant with the cavity mode [53–56]. Similar results have been shown for quantum dots near the band edge of two dimensional photonic crystals [57, 58]. Spontaneous emission rate enhancement and suppression of CdSe quantum dots coupled to band-edge modes of three dimensional photonic crystals have also been demonstrated [59].

Here, we demonstrate spontaneous emission rate enhancement and saturable absorption of CdSe(ZnS) colloidal quantum dots coupled to a nanobeam photonic

crystal cavity. Using time-resolved measurements, we show an average spontaneous emission rate enhancement of 4.6 for an ensemble of quantum dots located at the cavity. We also demonstrate cavity linewidth narrowing due to quantum dot saturable absorption. These results represent an important step towards development of integrated nanophotonic devices operating at room temperature.

## 3.2 Time-resolved lifetime measurements

Nanobeam photonic crystal cavities have been extensively studied numerically [23, 31, 60], and have been experimentally demonstrated in a number of previous works [21,24,25,28]. We utilize a cavity design proposed by Khan et al. [25]. Figure 3.1(a) shows the device structure and the calculated mode profile for the cavity. We calculate the cavity mode using numerical three dimensional finite-difference time-domain simulations (Lumerical Solutions). The cavity design consists of a 200-nm-thick and 300-nm-wide silicon nitride (SiN) beam with a one-dimensional periodic array of air holes ($a$ = 250 nm and $r$ = 70 nm). The cavity is formed by linearly reducing the lattice constant from $a$ = 250 nm to $a_0$ = 205 nm and the hole radius from $r$ = 70 nm to $r_0$ = 55 nm over a span of 4 holes at the center of the beam (symmetrically on both sides).

We fabricate the device on 200-nm-thick stoichiometric SiN and the fabrication procedure is discussed in detail in Chapter 2. A scanning electron microscope image of a fabricated device is shown in Fig. 3.1(b). We disperse CdSe(ZnS) (Invitrogen Qtracker CdSe/ZnS 655 nm) quantum dots on the device by drop-casting a 10 nM

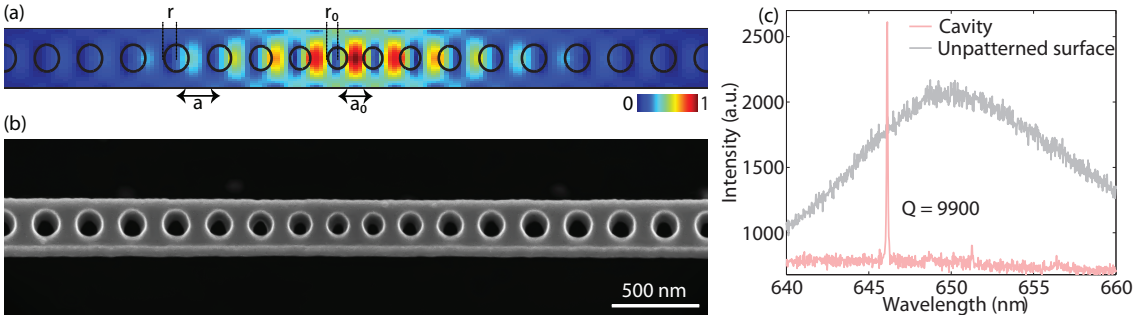


Figure 3.1: (a) Electric field intensity ($|E|^2$) profile of the resonant cavity mode. (b) Scanning electron microscope image of a nanobeam photonic crystal cavity. (c) Photoluminescence-spectra of CdSe (ZnS) colloidal quantum dots located at the cavity and on unpatterned silicon nitride surface at room temperature.

aqueous solution and dabbing off the excess solution after 10 minutes. We note that due to this deposition technique, the quantum dots are not dispersed uniformly on the surface of the devices. Using atomic force microscopy, we determine the average density of the quantum dots on a nanobeam to be $\approx$50 $\mu$m$^{-2}$.

To avoid oxidation and photo-bleaching of the quantum dots during the experiment, we load the device into a sealed chamber filled with purified nitrogen gas. For lifetime measurements, we illuminate the sample with 70 ps laser pulses at 405 nm wavelength and a repetition rate of 5 MHz (PDL800B, LDH-P-C-405B, PicoQuant). We set the average power to 500 nW to avoid creation of biexcitons and, thus, minimize the effect of excitation power on the measured lifetimes [61]. The laser excitation spot is about 1 $\mu$m in diameter. The photoluminescence signal from the sample is collected using an objective lens with numerical aperture of 1.3. Of the collected signal, 25% is used for imaging and the rest is split equally

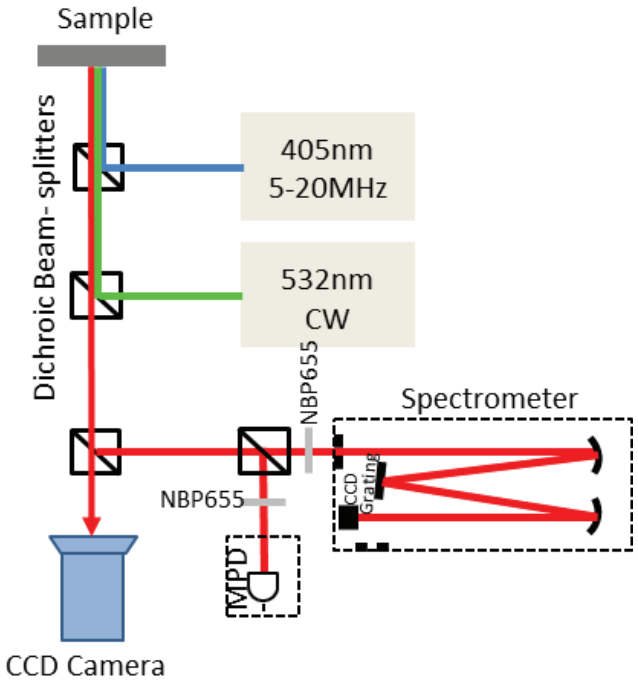


Figure 3.2: Schematic of the experimental setup. NBP = narrow band-pass filter

between a grating spectrometer and a photon counting module (Picoquant MPD along with Picoharp 300) for simultaneous spectral and time-resolved lifetime measurements (shown in Fig. 3.2). We use a spatial filter to collect light only from a 1 $\mu$m region around the cavity, and a spectral filter with 40 nm bandwidth (Semrock FF01-655/40-25) to reject all light outside the quantum dot bandwidth.

Figure 3.1(c) shows typical photoluminescence spectra obtained by exciting the cavity region as well as an unpatterned region away from the nanobeam. The spectrum of ensemble of quantum dots located on an unpatterned region exhibits a broad homogenous linewidth of 21 nm. In contrast, the cavity spectrum exhibits a bright peak at the cavity resonant wavelength of 646.1 nm. We fit the cavity spectrum to a Lorentzian function to determine a quality factor of $Q = 9900$.

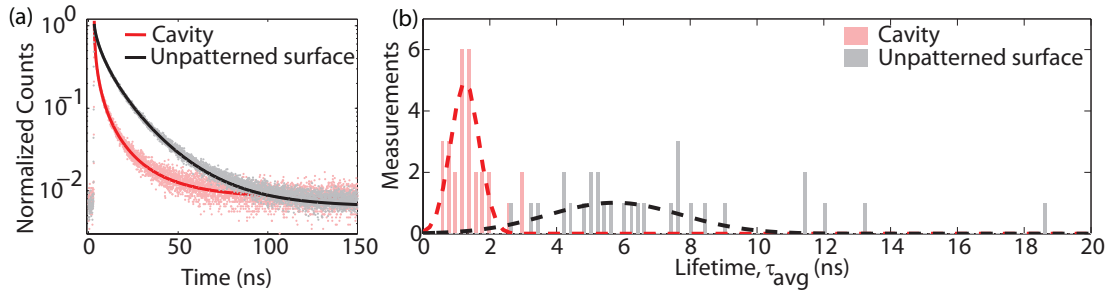


Figure 3.3: (a) Time-resolved lifetime measurements of the quantum dots located at the cavity and on unpatterned silicon nitride surface (spectra shown in Fig. 3.1(c)). The stretched exponential fits are shown by solid curves. (b) Histogram of the lifetime ($\tau_{avg}$ from stretched exponential fit) from 29 different devices from 3 separately fabricated samples. The Gaussian fits are shown by dashed curves.

Figure 3.3(a) plots time-resolved lifetime measurement of the quantum dot emission collected from the cavity and an unpatterned region away from the nanobeam. We normalize the curves with respect to their count rates at time $t = 0$. The cavity fluorescence decays faster than the fluorescence from the unpatterned surface. Both temporal decays (on and off the cavity) exhibit a multi-exponential behavior. Multi-exponential decays in quantum dots have been previously studied and attributed to temporal fluctuations in non-radiative relaxation pathways due to changes in electronic or structural environment of the quantum dots [62, 63]. Cavities can induce additional fluctuations through variations in quantum dot positions and dipole orientations relative to the cavity field, which leads to different spontaneous emission enhancements [59, 64].

Two main decay models have been proposed for studying multi-exponential

decay processes: stretched exponential fit [63] and log-normal fit [64,65]. Here we use a stretched exponential fit given by

$$I(t) = I_0 + Ae^{-(t/\tau_{se})^{\beta}} \tag{3.1}$$

where $I(t)$ is the photoluminescence intensity at time $t$, $I_0$ is the background intensity level, $\tau_{se}$ is the $1/e$ decay lifetime, $\beta$ is the stretch parameter, and $A$ is a scaling constant. The stretch parameter $\beta$ ranges between 0 and 1, and is inversely related to the variance of the decay rate ($\beta = 1$ corresponds to a single-exponential). From the stretched exponential fit, the average decay lifetime of the ensemble can be calculated by

$$\tau_{avg} = \frac{\tau_{se}}{\beta}\Gamma\left(\frac{1}{\beta}\right) \tag{3.2}$$

where $\Gamma$ is the Gamma function.

We fit the lifetime data shown in Fig. 3.3(a) to Eq. (3.1) by treating $\tau_{se}$, $\beta$, and $A$ as fitting parameters. The solid lines in Fig. 3.3(a) represent the fitted values. These fits correspond to $\tau_{se} = 0.32$ ns and $\beta = 0.36$ for quantum dots located at the cavity, and $\tau_{se} = 5.35$ ns and $\beta = 0.62$ for quantum dots located on the unpatterned silicon nitride surface. The $\beta$ from the fit on the cavity data is smaller than the one from the unpatterned surface because the cavity creates an additional fluctuation in lifetime of quantum dots due spatial variation in cavity mode. Using Eq. (3.2), we calculate the average lifetime, $\tau_{avg}$, for quantum dots located at the cavity to be 1.5 ns and quantum dots located at unpatterned silicon nitride surface to be 7.66 ns.

We performed lifetime measurements on 29 different devices from 3 separately

fabricated samples. Figure 3.3(b) plots $\tau_{avg}$ for all these measurements. The dashed curves are Gaussian fits to both the lifetime distributions. We observe a mean lifetime of 1.25 ns for quantum dots located at the cavity and 5.74 ns for quantum dots located on unpatterned silicon nitride surface, leading to an average spontaneous emission rate enhancement of 4.6. For quantum dots on the unpatterned surface we observe a shorter lifetime than those typically reported for single quantum dots deposited on glass [63, 66]. This reduction may be caused by modification of the local density of states due to the larger dielectric constant of SiN [67,68] and Forster energy transfer between quantum dots [69]. Nonradiative decay may also contribute to the measured lifetimes. Because quantum dots are deposited on the device after the fabrication process, they are expected to have the same non-radiative decay rate regardless of whether they are deposited on the cavity or the unpatterned surface. In this case, the measured decrease in lifetime provides a lower bound on the actual spontaneous emission enhancement factor.

## 3.3 Simulation Results

The spontaneous emission enhancement factor for a quantum dot located at position $\mathbf{r}$ in the cavity, defined as $F(\mathbf{r}) = \gamma(\mathbf{r})/\gamma_0$ where $\gamma(\mathbf{r})$ is the decay rate of the quantum dot located at the cavity and $\gamma_0$ in free space, assuming the dipole transition is resonant and emitting in the same polarization as the cavity mode is given by [70]:

$$F(\mathbf{r}) = 1 + \frac{3\lambda^3}{4\pi^2 n^2}\frac{Q_{qd}}{V}\psi(\mathbf{r}) \tag{3.3}$$

In the above equation, $\lambda$ is the cavity-mode wavelength, $Q_{qd} = \lambda/\Delta\lambda_{qd}$ is the quantum dot quality factor, $\Delta\lambda_{qd}$ is the quantum dot linewidth, $n$ is the refractive index of the cavity dielectric, $V = \int d^3\mathbf{r}\epsilon(\mathbf{r})|E(\mathbf{r})|^2/[\epsilon(\mathbf{r})|E(\mathbf{r})|^2]_{max}$ is the cavity mode volume, $\epsilon(\mathbf{r})$ is the relative dielectric constant, and $\psi(\mathbf{r}) = |E(\mathbf{r})|^2/[|E(\mathbf{r})|^2]_{max}$ is the ratio of cavity-field intensity at location $\mathbf{r}$ to the maximum cavity field intensity. We note that the above equation is different from the conventional expression for the spontaneous emission rate enhancement factor and depends on the quality factor of the quantum dot, not the quality factor of the cavity. This difference is attributed to the fact that the homogeneous linewidth of the quantum dots is broader than the cavity, and therefore, our cavity-quantum dot system lies in the bad emitter limit [52, 71].

We set the SiN refractive index to $n = 2.01$ [72] and single quantum dot linewidth to $\Delta\lambda_{qd} = 15$ nm [73]. Using finite-difference time-domain simulations, we calculate $V = 0.57(\lambda/n)^3$, $\lambda = 642.6$ nm, and $\psi = 0.355$ for a quantum dot located at the field maximum on the top surface of the nanobeam cavity. Plugging these values into Eq. (5.1), the maximum spontaneous emission rate enhancement is calculated to be 5.1. The calculated value for the spontaneous emission rate enhancement agrees with the measured value of 4.6.

# Chapter 4: Saturable Absorption

## 4.1 Introduction

Just as the cavity can affect the quantum dots by enhancing spontaneous emission, the quantum dots can affect the cavity through absorption which degrades the cavity Q. Because quantum dots saturate at high pump intensity, the cavity will exhibit an intensity-dependent linewidth. Saturable absorbers in a cavity can create enhanced nonlinear optical effects such as optical bistability [11–14], optical switching [18, 20], and passive mode locking [74].

## 4.2 Experiment

In order to create sufficient quantum dot absorption to decrease Q, we increase the quantum dot density by performing five deposition steps on the device, as opposed to the single deposition step used for lifetime measurements. Using atomic force microscopy, we determine the average quantum dot density on a nanobeam to be $\approx 250\ \mu\text{m}^{-2}$. We increased the pulsed laser repetition rate to 20 MHz to get higher signal. The collected photoluminescence signal is sent to a grating spectrometer to measure the cavity spectrum. Figure 4.1(a) shows the normalized cavity

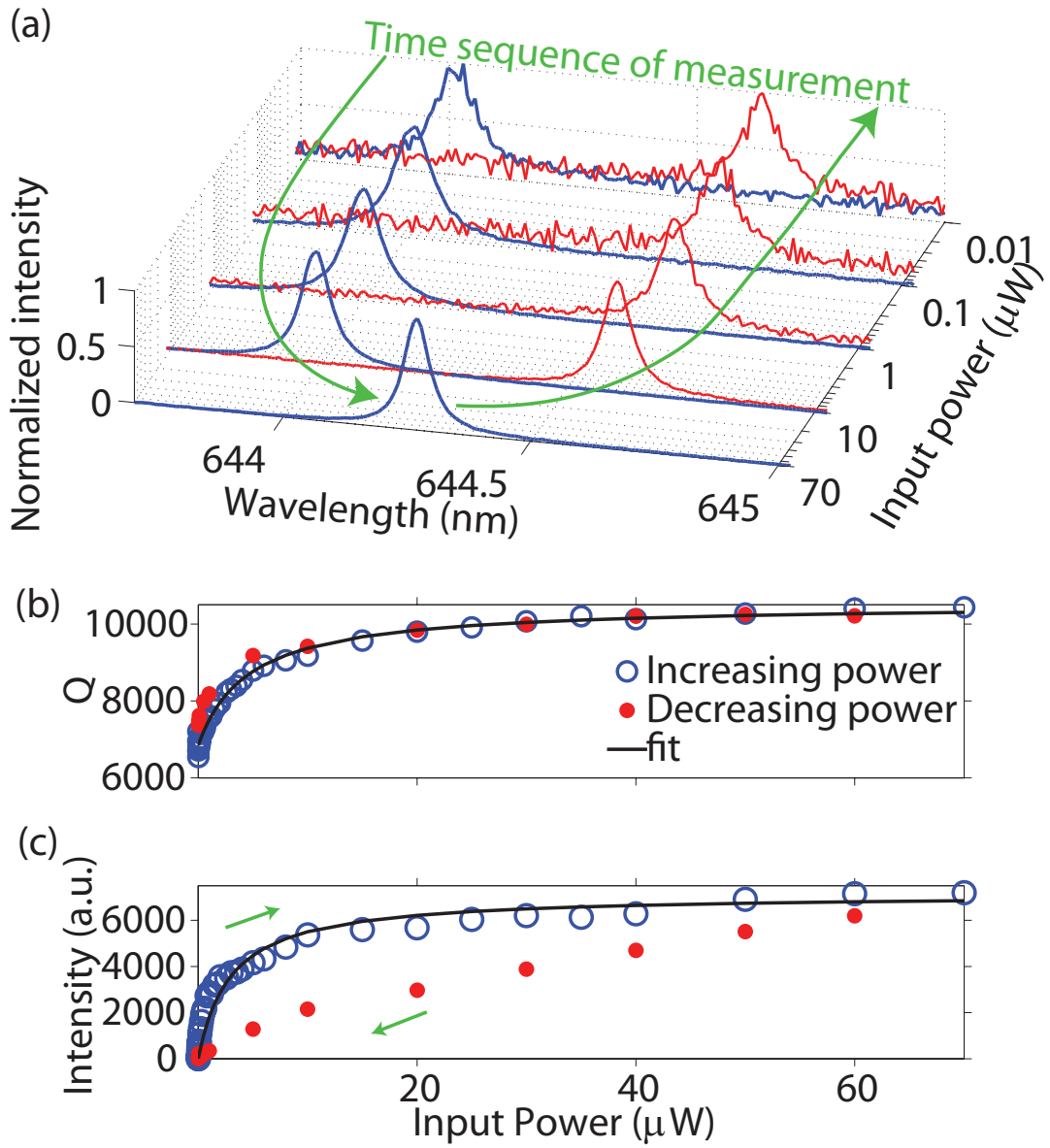


Figure 4.1: (a) Normalized cavity spectrum for different input pump power levels. The green curved arrows show the time sequence in which the cavity spectra were measured. (b) Cavity Q as a function of input pump power. (c) Integrated cavity photoluminescence intensity as a function of input pump power.

spectrum for several different input powers (the green arrows show the time sequence in which the cavity spectra were measured). We gradually increase the input power from 10 nW to 70 $\mu$W, and the corresponding spectra are shown in blue. Once the input power level is at 70 $\mu$W, we gradually decrease the input power back to 10 nW, and the corresponding spectra are shown in red. We observe that the cavity spectrum narrows with higher input power and becomes broad again when the input power is decreased back. We also observe an irreversible shift in resonance wavelength at higher input powers, which may be caused by photo-induced damage to the quantum dots [73] or cavity membrane at high intensities.

Figure 4.1(b) plots the cavity Q as a function of input power, determined by performing a Lorentzian fit to the cavity spectrum. The blue circles show the cavity Q when the input power is gradually increased from 10 nW to 70 $\mu$W, and the red dots represent the Q when the input power is gradually decreased back to 10 nW. In the increasing power cycle, Q increases from 6700 at 10 nW to 10400 at 70 $\mu$W. The increase in cavity Q as a function of pump power is due to quantum dot saturation, which reduces the absorption in the cavity. In the decreasing power cycle, the cavity Q does not fully recover to its original value, but reaches a slightly higher value of 7400. This behavior is attributed to photo bleaching of quantum dots at higher powers during the increasing power cycle, which leads to a slightly lower absorption. The solid curve, in Fig. 4.1(b), is a fit to a model based on a cavity coupled to a homogeneous saturable absorber, where Q is given by [75]:

$$\frac{1}{Q} = \frac{1}{Q_c} + \frac{1}{Q_{ab}} \frac{1}{1 + P/P_{sat}} \tag{4.1}$$

where $Q_c$ is the quality factor of the bare cavity, $Q_{ab}$ is the quality factor due to quantum dot absorption at low (unsaturated) powers, $P$ is the input power, and $P_{sat}$ is the saturation power. We fit the quality factor data, obtained for the increasing power cycle, to the above equation, treating $Q_c$, $Q_{ab}$ and $P_{sat}$ as fitting parameters. We obtain the best fit, shown as a solid curve in Fig. 4.1(b), for $Q_c = 10500$, $Q_{ab} = 19600$, and $P_{sat} = 2.98$ $\mu$W.

The cavity emission intensity provides further evidence that saturable absorption is the dominant mechanism for linewidth narrowing. Figure 4.1(c) plots the integrated cavity photoluminescence intensity as a function of input power, determined by performing a Lorentzian fit to the cavity spectrum. The blue circles represent the intensity when the input power is gradually increased from 10 nW to 70 $\mu$W, and the red dots represent the intensity when the input power is gradually decreased back to 10 nW. The integrated cavity photoluminescence intensity increases linearly with increasing input power and eventually saturates. The solid curve in Fig. 4.1(c) is a fit to a saturable absorption model given by [76]

$$I_c = \frac{\alpha P}{1 + P/P_{sat}} \tag{4.2}$$

where $I_c$ is the photoluminescence intensity and $\alpha$ is a proportionality constant. Figure 4.1(c) shows the best-fit results where we treat $\alpha$ as a fitting parameter and use the calculated $P_{sat}$ from Eq. (4.1). The fit is performed for the data obtained for increasing power cycle, and exhibits good agreement with the experimental measurements. Both the intensity and the cavity Q saturate with the same $P_{sat}$, providing strong support for saturable absorption as the dominant mechanism for the intensity

dependent cavity linewidth.

When the power is decreased back down, the observed intensity values during the decreasing power cycle are lower than those in the increasing power cycle. This behavior is irreversible, it does not recover when we increase the power back up on subsequent power cycles but instead further degrades. It is therefore not due to power hysteresis effects such as thermal or optical bistability, which typically require direct resonant excitation of the cavity mode. This reduction in intensity is caused by photo-bleaching of quantum dots at higher input powers, and is also consistent with the fact that $Q$ does not drop down completely to its original value (Fig. 4.1(b)).

# Chapter 5: Overcoming Auger recombination in nanocrystal quantum dot laser using spontaneous emission enhancement

## 5.1 Introduction

Room-temperature nanolasers have applications in fields ranging from optical communications and information processing [77] to biological sensing [78] and medical diagnostics [79]. Colloidally synthesized nanocrystal quantum dots are a promising gain material for nanolasers. These quantum dots are efficient emitters at room temperature [51, 80], have broadly tunable emission frequencies [33, 81] and are easy to integrate with photonic structures [47–49].

Nanocrystal quantum dot lasers have been demonstrated using resonant structures such as distributed feedback gratings [49], microspheres [47], and micro-toroids [48]. However, these devices have exhibited high lasing thresholds due to fast non-radiative decay caused by Auger recombination [82, 83]. Nanocrystal quantum dots have a fast Auger recombination rate owing to the tight spatial confinement of carriers [83]. One approach to reduce Auger recombination is by engineering quantum dots with decreased spatial confinement. For example, elongated nanocrystals (quantum rods) can reduce Auger recombination [84, 85] to achieve lower thresh-

old lasing [86]. Core/shell heteronanocrystals may also reduce the carrier spatial confinement [87,88], but have yet to be successfully integrated into a laser structure.

Here we show that spontaneous emission rate enhancement in a small mode volume cavity [10] can overcome Auger recombination and enable low threshold lasing. We derive a model for a nanocrystal quantum dot laser using a master equation formalism that accounts for both Auger recombination and spontaneous emission enhancement. Using this model we show that spontaneous emission enhancement reduces the effect of Auger recombination, resulting in up to a factor of 17 reduction in the lasing threshold. We analyze a nanobeam photonic crystal cavity as a promising device implementation to achieve low threshold lasing in the presence of Auger recombination.

In section 5.2 we derive the theoretical formalism for a nanocrystal quantum dot laser. Section 5.3 presents numerical calculations for a general cavity structure under the uniform-field approximation. In section 5.4 we propose and analyze a nanobeam photonic crystal cavity design as a potential device implementation of a nanocrystal quantum dot laser.

## 5.2 Derivation of numerical model

Figure 5.1(a) illustrates the general model for a nanocrystal quantum dot laser. The laser is composed of an ensemble of quantum dots coupled to a single cavity mode. The level structure of the quantum dots, shown in Fig. 5.1(b), consists of four states: a ground state $|1\rangle$ which contains no carriers, the single exciton states $|2\rangle$

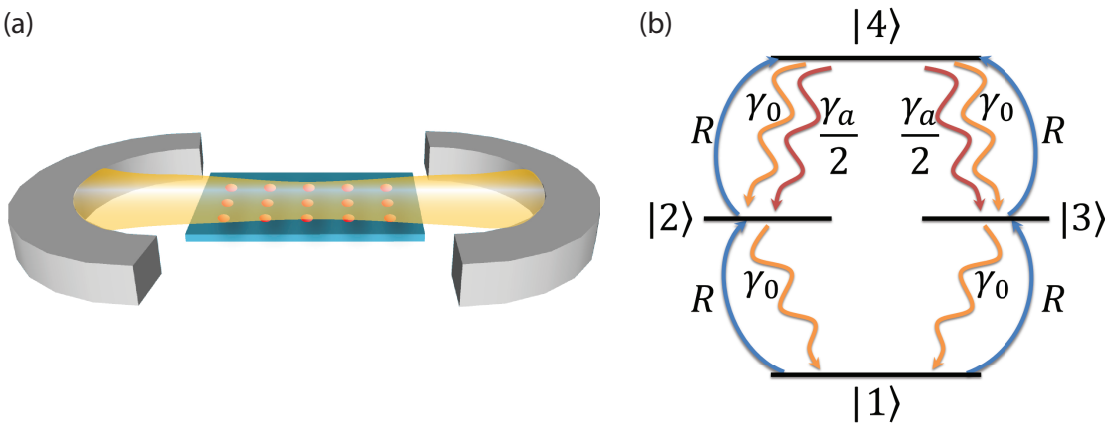


Figure 5.1: (a) Schematic of a laser composed of nanocrystal quantum dots coupled to an optical cavity. (b) Level diagram for a four-level model of a nanocrystal quantum dot.

and $|3\rangle$ which contain a single electron-hole pair, and the biexciton state $|4\rangle$ which contains two electron-hole pairs. In the single exciton states, the quantum dot absorbs and emits a photon with nearly equal probability. Thus, only the biexciton state can provide optical gain [34]. However, this state suffers from Auger recombination where an electron-hole pair recombines and transfers energy non-radiatively to a third carrier [83]. The strong carrier confinement in the quantum dots leads to fast Auger recombination, resulting in a low biexciton radiative efficiency.

Figure 5.1(b) also shows the relevant decay rates for our quantum dot model. The biexciton state decays to each exciton state with the rate $\gamma_2 = \gamma_0 + \gamma_a/2$, where $\gamma_0$ is the spontaneous emission rate and $\gamma_a$ is the total Auger recombination rate of the biexciton state. We assume the single exciton states decay predominantly by spontaneous emission. We also assume equal spontaneous emission rates for all

four allowed transitions, and ignore long-lived trap states that are responsible for blinking behavior [89, 90]. These states can be incorporated as additional energy levels in the model. The quantum dot is incoherently pumped with an external source characterized by the excitation rate $R$.

In bare nanocrystal quantum dots Auger recombination is an order of magnitude faster than spontaneous emission [83]. It therefore dominates the decay of the biexciton state and quenches the optical gain. However, when the quantum dot spectrally couples to an optical cavity, its spontaneous emission rate increases by the factor [52].

$$F(\mathbf{r}_0) = 1 + \frac{2g^2(\mathbf{r}_0)}{\gamma_0 K_{XX}} \tag{5.1}$$

where $g(\mathbf{r}_0)$ is the cavity-quantum dot coupling strength given by

$$g(\mathbf{r}_0) = \frac{\mu \cdot \hat{\mathbf{e}}}{\hbar}\sqrt{\frac{\hbar\omega_c}{2\epsilon_0 V_m}}\frac{|E(\mathbf{r}_0)|}{|E(\mathbf{r})|_{max}} \tag{5.2}$$

Here, $E(\mathbf{r}_0)$ is the electric field amplitude, $\hat{\mathbf{e}}$ is the polarization direction of the cavity mode at the quantum dot position $\mathbf{r}_0$, $\omega_c$ is the cavity mode resonant frequency, $V_m = \int d^3\mathbf{r}\epsilon(\mathbf{r})|E(\mathbf{r})|^2/[|E(\mathbf{r})|^2]_{max}$ is the cavity mode-volume [91], $\epsilon_0$ is the permittivity of free space, $\epsilon(\mathbf{r})$ is the relative dielectric permittivity and $\mu$ is the quantum dot dipole moment. The rate $K_{XX} = (\gamma_0 + 2\gamma_2 + \gamma_d)/2$ represents the total linewidth of the biexciton state, which is dominated by the dephasing rate $\gamma_d$ at room-temperature [66, 73, 83]. We note that Eq. (5.1) is different from the more common expression for $F$ that depends on the ratio of the cavity quality factor $Q$ and the cavity mode-volume $V_m$ [10, 52]. This difference occurs because at room temperature the dephasing rate of nanocrystal quantum dots is much larger

than the cavity linewidth. The device therefore operates in the bad emitter regime, where $F$ becomes independent of the cavity $Q$. By engineering cavities with small mode-volumes, we can achieve large $F$ and enhance the spontaneous emission rate, thereby increasing the radiative efficiency of the quantum dot in the presence of Auger recombination.

To analyze the nanocrystal quantum dot laser in the presence of Auger recombination and spontaneous emission enhancement, we begin with the master equation

$$\frac{\partial \rho}{\partial t} = \frac{i}{\hbar}[\rho, \mathbf{H}] + \mathbf{L}\rho \tag{5.3}$$

where $\rho$ is the density matrix of the combined cavity-quantum dot system, $\mathbf{H}$ is the Hamiltonian, and $\mathbf{L}$ is the Liouvillian superoperator that accounts for incoherent damping and excitation processes. The Hamiltonian of the system is given by $\mathbf{H_{cavity}} + \mathbf{H_{NQD}} + \mathbf{H_{JC}}$, where

$$\begin{aligned}
\mathbf{H_{cavity}} &= \hbar\omega_c \mathbf{a}^\dagger \mathbf{a} && (5.4)\\
\mathbf{H_{NQD}} &= \sum_{m=1}^{N} \hbar\omega_m^X(\sigma_{22,m} + \sigma_{33,m}) + \hbar\omega_m^{XX}\sigma_{44,m} && (5.5)\\
\mathbf{H_{JC}} &= \sum_{i=m}^{N} \hbar g_m^X(\mathbf{r}_m)(\sigma_{21,m}\mathbf{a} + \sigma_{12,m}\mathbf{a}^\dagger + \sigma_{31,m}\mathbf{a} + \sigma_{13,m}\mathbf{a}^\dagger) \\
&+ \hbar g_m^{XX}(\mathbf{r}_m)(\sigma_{42,m}\mathbf{a} + \sigma_{24,m}\mathbf{a}^\dagger + \sigma_{43,m}\mathbf{a} + \sigma_{34,m}\mathbf{a}^\dagger) && (5.6)
\end{aligned}$$

In the above equations $\mathbf{a}$ and $\mathbf{a}^\dagger$ are the bosonic annihilation and creation operators of the cavity mode. The summation is carried out over all quantum dots in the cavity, where we denote the total number of quantum dots by $N$. For the $m^{th}$ quantum dot, $\sigma_{jk,m} = |j\rangle\langle k|$ represents the atomic dipole operator when $j \neq k$ and the atomic population operator when $j = k$, for the single exciton states ($j = 2, 3$)

and the biexciton state ($j = 4$). We set the energy of the quantum dot ground state to zero. We define $\omega_m^X$ and $\omega_m^{XX}$ as the resonant frequencies of the single-exciton and biexciton transitions, respectively. Similarly, the cavity-quantum dot coupling strengths for the exciton and biexciton transitions are $g_m^X(\mathbf{r}_m)$ and $g_m^{XX}(\mathbf{r}_m)$ for the $m^{th}$ quantum dot at position $\mathbf{r}_m$. At room temperature, the homogenous linewidth of these quantum dots is much larger than the biexcitonic shift [92–95]. We therefore assume all four transitions of each quantum dot are resonantly coupled to the cavity mode ($\omega_c = \omega_m^X = \omega_m^{XX}/2$). The Liouvillian superoperator $\mathbf{L}$ is fully defined in Appendix A.1.

The master equation is difficult to solve both analytically and numerically when the number of quantum dots becomes large. However, we can simplify the calculations by applying the semi-classical approximation in which the coherence between the atoms and the field is neglected [96, 97] and the density matrix can be factorized into a product of the state of the field and atoms (see Appendix A.2). Under this approximation, the system is described by the average cavity photon number, $p$, and the quantum dot population density, $n_j(\mathbf{r}) = \lim_{\Delta V \to 0} \sum_m \langle \sigma_{jj}^m \rangle / \Delta V$, where the sum is carried out over all quantum dots contained in a small volume $\Delta V$ at location $\mathbf{r}$. We note that $n_j(\mathbf{r})$ is a function of the position $\mathbf{r}$ inside the cavity because of the non-uniform cavity field distribution. We derive the equations of motion of $n_j(\mathbf{r})$ from the master equation (see Appendix A.2) as

$$\frac{\partial n_1(\mathbf{r})}{\partial t} = \Gamma_X(\mathbf{r})[(p+1)(n_2(\mathbf{r}) + n_3(\mathbf{r})) - 2pn_1(\mathbf{r})] + \gamma_0[n_2(\mathbf{r}) + n_3(\mathbf{r})] - 2Rn_1(\mathbf{r}) \quad (5.7)$$

$$\frac{\partial n_2(\mathbf{r})}{\partial t} = -\Gamma_X(\mathbf{r})[(p+1)n_2(\mathbf{r}) - pn_1(\mathbf{r})] + \Gamma_{XX}(\mathbf{r})[(p+1)n_4(\mathbf{r}) - pn_2(\mathbf{r})]$$

$$- \quad \gamma_0 n_2(\mathbf{r}) + \gamma_2 n_4(\mathbf{r}) + R[n_1(\mathbf{r}) - n_2(\mathbf{r})] \tag{5.8}$$

$$\frac{\partial n_3(\mathbf{r})}{\partial t} = -\Gamma_X(\mathbf{r})[(p+1)n_3(\mathbf{r}) - pn_1(\mathbf{r})] + \Gamma_{XX}(\mathbf{r})[(p+1)n_4(\mathbf{r}) - pn_3(\mathbf{r})]$$

$$- \quad \gamma_0 n_3(\mathbf{r}) + \gamma_2 n_4(\mathbf{r}) + R[n_1(\mathbf{r}) - n_3(\mathbf{r})] \tag{5.9}$$

$$\frac{\partial n_4(\mathbf{r})}{\partial t} = -\Gamma_{XX}(\mathbf{r})[2(p+1)n_4(\mathbf{r}) - p(n_2(\mathbf{r}) + n_3(\mathbf{r}))] - 2\gamma_2 n_4(\mathbf{r})$$

$$+ \quad R[n_2(\mathbf{r}) + n_3(\mathbf{r})] \tag{5.10}$$

In the above equations, $\Gamma_X(\mathbf{r}) = 2g^2(\mathbf{r})/K_X$ and $\Gamma_{XX}(\mathbf{r}) = 2g^2(\mathbf{r})/K_{XX}$ are the modified spontaneous emission rates of the single-exciton and biexciton transitions, where $K_X = (\gamma_0 + \gamma_d + 3R)/2$ and $K_{XX} = (\gamma_0 + 2\gamma_2 + \gamma_d + R)/2$. Here, we assume equal coupling strength for the single-exciton and biexciton transitions. We also treat the quantum dots in a small volume $\Delta V$ of the cavity to be identical, and therefore drop the subscript $m$ from the coupling strength ($g(\mathbf{r}) = g_m^X(\mathbf{r}_m) = g_m^{XX}(\mathbf{r}_m)$).

The average cavity photon number satisfies a rate equation given by (see Appendix A.3 for derivation)

$$\frac{\partial p}{\partial t} = -p\kappa + pG(p) + \alpha(p) \tag{5.11}$$

where $\kappa = \omega_c/Q$ is the cavity energy decay rate. The above equation is coupled to the quantum dot population density rate equations through the cavity gain coefficient

$$G(p) = \int d^3\mathbf{r} \left\{\Gamma_X(\mathbf{r})[n_2(\mathbf{r}) + n_3(\mathbf{r}) - 2n_1(\mathbf{r})] + \Gamma_{XX}(\mathbf{r})[2n_4(\mathbf{r}) - n_2(\mathbf{r}) - n_3(\mathbf{r})]\right\} \tag{5.12}$$

and the spontaneous emission rate into the lasing mode

$$\alpha(p) = \int d^3\mathbf{r} \left\{\Gamma_X(\mathbf{r})[n_2(\mathbf{r}) + n_3(\mathbf{r})] + 2\Gamma_{XX}(\mathbf{r})n_4(\mathbf{r})\right\} \tag{5.13}$$

where the integral is over all space. We use the notation $G(p)$ and $\alpha(p)$ to highlight the fact that the above coefficients have a $p$ dependence because the atomic densities $n_j(\mathbf{r})$ depend on the cavity photon number. The absorbed pump power of the nanocrystal quantum dot laser is given by

$$P_{abs} = \hbar\omega_p R \int_{V_p} d^3\mathbf{r}[2n_1(\mathbf{r}) + n_2(\mathbf{r}) + n_3(\mathbf{r})] \tag{5.14}$$

where $\omega_p$ is the pump frequency and $V_p$ is the optically pumped volume. The output power of the laser is given by

$$P_{out} = \hbar\omega_c p\kappa \tag{5.15}$$

An important figure of merit for small mode-volume cavities is the spontaneous emission coupling efficiency, denoted by $\beta$ (Note: This $\beta$ is different from the one used in Chapter 3 for stretched exponential fit.). This parameter quantifies the fraction of photons spontaneously emitted to the cavity mode. A $\beta$ approaching unity achieves thresholdless lasing [1]. In the quantum dot model, the single exciton and biexciton transitions have different coupling efficiencies given by

$$\beta_X(\mathbf{r}) = \frac{\Gamma_X(\mathbf{r})}{\Gamma_X(\mathbf{r}) + \gamma_0} \tag{5.16}$$

$$\beta_{XX}(\mathbf{r}) = \frac{\Gamma_{XX}(\mathbf{r})}{\Gamma_{XX}(\mathbf{r}) + \gamma_2} \tag{5.17}$$

The above coupling efficiencies depend on the position $\mathbf{r}$ due to the spatially varying cavity field intensity. The rate equations Eqs. (5.7)-(5.11) describe the dynamics of a general nanocrystal quantum dot laser. We will use these equations in the remaining sections.

## 5.3 Lasing analysis under uniform-field approximation

The general cavity-quantum dot rate equation model, developed in the previous section, is still difficult to solve due to the spatial variation of the coupling strength $g(\mathbf{r})$. This spatial variation leads to a complex set of coupled differential equations for each position inside the cavity volume. We note that this complexity is not unique to the system we study. It occurs in virtually all laser systems and is responsible for effects such as spatial hole burning [75]. One way to simplify the problem is to make the uniform-field approximation, where we replace $\Gamma_i(\mathbf{r})$ (i = X, XX) in Eqs. (5.7)- (5.14) with its spatially averaged value

$$\bar{\Gamma}_i = \frac{1}{V_m}\int d^3\mathbf{r}\Gamma_i(\mathbf{r}) = \frac{2g_o^2}{K_i} \tag{5.18}$$

where $g_o = \mu \cdot \hat{\mathbf{e}}\sqrt{\omega_c/2\hbar\epsilon_o\epsilon_{eff}V_m}$ and

$$\epsilon_{eff} = \frac{\int d^3\mathbf{r}|E(\mathbf{r})|^2\epsilon(\mathbf{r})}{\int d^3\mathbf{r}|E(\mathbf{r})|^2} \tag{5.19}$$

Under the uniform field approximation the atomic population densities $n_j(\mathbf{r})$ are no longer spatially varying. We can therefore express the equations of motion in terms of the total number of quantum dots in state $j$ given by $N_j = V_m n_j$ where $V_m$ is the cavity mode volume. These quantum dot populations must satisfy the constraint that $\sum_j N_j = N$, where $N$ is the total number of quantum dots contained in the cavity. With these definitions, the equations of motion become the standard cavity-atom rate equations, given by

$$\frac{\partial N_1}{\partial t} = \bar{\Gamma}_X[(p+1)(N_2+N_3) - 2pN_1] + \gamma_0(N_2+N_3) - 2RN_1 \tag{5.20}$$

$$\frac{\partial N_2}{\partial t} = -\bar{\Gamma}_X[(p+1)N_2 - pN_1] + \bar{\Gamma}_{XX}[(p+1)N_4 - pN_2] - \gamma_0 N_2 + \gamma_2 N_4$$
$$+ R(N_1 - N_2) \tag{5.21}$$
$$\frac{\partial N_3}{\partial t} = -\bar{\Gamma}_X[(p+1)N_3 - pN_1] + \bar{\Gamma}_{XX}[(p+1)N_4 - pN_3] - \gamma_0 N_3 + \gamma_2 N_4$$
$$+ R(N_1 - N_3) \tag{5.22}$$
$$\frac{\partial N_4}{\partial t} = -\bar{\Gamma}_{XX}[2(p+1)N_4 - p(N_2 + N_3)] - 2\gamma_2 N_4 + R(N_2 + N_3) \tag{5.23}$$
$$\frac{\partial p}{\partial t} = -p\kappa + p\bar{G}(p) + \bar{\alpha}(p) \tag{5.24}$$

where

$$\bar{G}(p) = \bar{\Gamma}_X(N_2 + N_3 - 2N_1) + \bar{\Gamma}_{XX}(2N_4 - N_2 - N_3) \tag{5.25}$$

and

$$\bar{\alpha}(p) = \bar{\Gamma}_X(N_2 + N_3) + 2\bar{\Gamma}_{XX}N_4 \tag{5.26}$$

are the gain coefficient and spontaneous emission rate into the lasing mode. The absorbed power is given by

$$\bar{P}_{abs} = \hbar\omega_p R(2N_1 + N_2 + N_3) \tag{5.27}$$

The output power of the laser is still given by Eq. (5.15).

We first determine the minimum number of quantum dots required to achieve lasing. We define $N_{th}$ as the total number of quantum dots in the cavity required to achieve a small signal gain equal to the cavity loss ($\lim_{p\to 0} \bar{G}(p) = \kappa$), and calculate it by using the analytical steady-state solutions to Eqs. (5.20)- (5.23) along with the condition $\sum_j N_j = N$ (see Appendices A.4, A.5). To perform calculations, we consider the specific example of colloidal CdSe/ZnS core-shell quantum dots that emit in a wavelength range of 500-700 nm. We perform simulations using a

dephasing rate of $\gamma_d = 4.39\times10^4$ ns$^{-1}$ [73], a spontaneous emission rate of $\gamma_0 = 1/18$ ns$^{-1}$ [66], and an Auger recombination rate of $\gamma_a = 1/300$ ps$^{-1}$ [83,98]. Nanocrystal quantum dots can be incorporated into photonic devices in a variety of ways such as spin-casting [48, 99–102] and immersion in liquid suspension [47, 103]. In these cases, the quantum dots reside on the surfaces of the devices, so we set $\epsilon_{eff} = 1$.

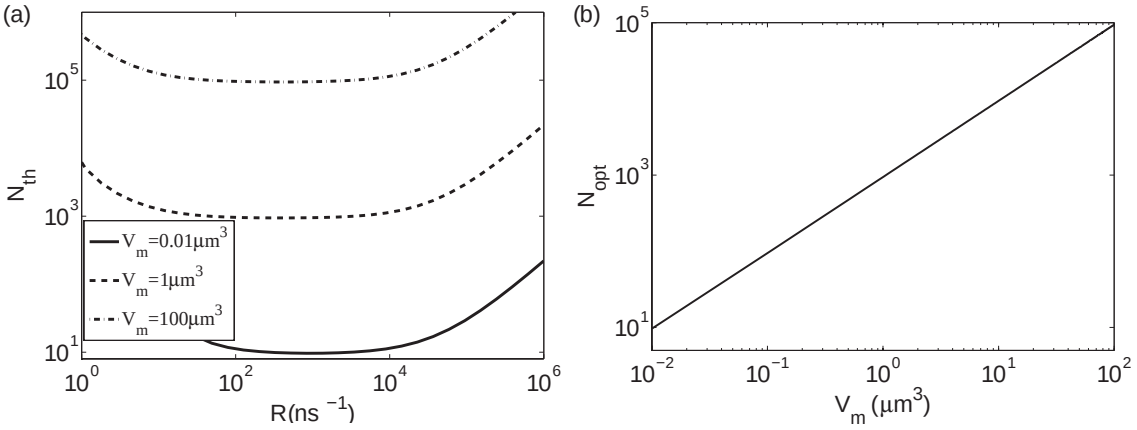


Figure 5.2: (a) $N_{th}$ as a function of pump rate for $V_m = 0.01\mu m^3$, 1 $\mu m^3$ and $100\mu m^3$, $\gamma_a = 1/300$ ps$^{-1}$. (b) $N_{opt}$ for different mode-volumes for $\gamma_a = 1/300$ ps$^{-1}$.

Figure 5.2(a) plots $N_{th}$ as a function of pump rate $R$ for $V_m = 0.01\mu m^3$, $1\mu m^3$ and $100\mu m^3$ and $\gamma_a = 1/300$ ps$^{-1}$. Each mode-volume exhibits an optimum pump rate where the threshold quantum dot number is minimum. We denote this minimum threshold quantum dot number by $N_{opt}$. Figure 5.2(b) plots $N_{opt}$ as a function of $V_m$. The figure shows that $N_{opt}$ scales linearly with mode-volume.

Next, we investigate the laser input-output power characteristics. We calculate the laser output power (using Eq. (5.15)) and the absorbed pump power (using Eq. (5.27)) using the numerical steady-state solutions to Eqs. (5.20)-(5.24). Figure 5.3(a) plots $P_{out}$ as a function of $\bar{P}_{abs}$ (also known as the light-in light-out

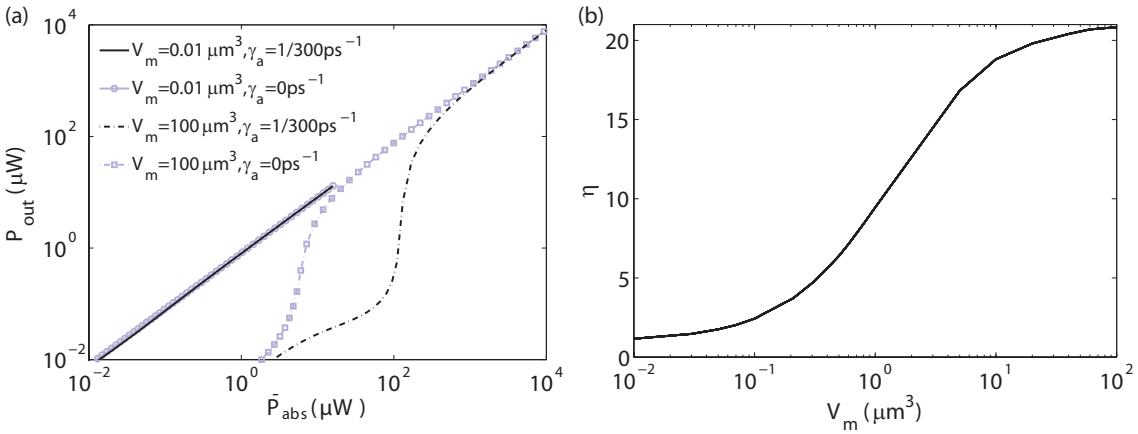


Figure 5.3: (a) Laser output power as a function of the absorbed pump power for $V_m = 0.01\mu m^3$ and $100\mu m^3$. (b)$\eta$ as a function of mode-volume.

curve), under the uniform-field approximation, for two different mode-volumes of $V_m = 0.01\ \mu m^3$ and $100\ \mu m^3$, as well as two different Auger recombination rates of $\gamma_a = 1/300\ \text{ps}^{-1}$ and 0. We set $Q = 20000$ and $N = 2N_{opt}$ (Fig. 5.2(b)) for each respective mode-volume. We calculate the curves in Fig. 5.3(a) using the same range of $R$ values for both the mode-volumes. We note that the curves for the small mode volume cavity terminate earlier than those of the large mode volume cavity because the number of quantum dots contained inside the cavity mode-volume is much lower, which reduces the maximum output power.

The cavities with $V_m = 100\mu\text{m}^3$, indicated by the dashed curves in Fig. 5.3(a), exhibit a pronounced threshold. Near threshold, the light-in light-out curve takes on the well-known S-curve behavior as it transitions from the below-threshold to above-threshold regime. Auger recombination increases the threshold by quenching the gain, which causes the S-curve region to occur at higher absorbed powers. Similar to $N_{th}$, we define the threshold power as the absorbed power where the small signal

gain equals the cavity loss. We calculate this value numerically using the steady state solutions to Eqs. (5.20)- (5.23), along with Eq. (5.27). The threshold power for $V_m = 100\ \mu m^3$ is 122.7 $\mu$W when $\gamma_a = 1/300$ ps$^{-1}$, and 5.9 $\mu$W when $\gamma_a = 0$. Auger recombination therefore increases the lasing threshold by a factor of 21. When the mode volume is $V_m = 0.01\ \mu m^3$ the light-in light-out curve exhibits a thresholdless lasing behavior. The output power is nearly a linear function of the input power. Using the same definition of threshold, we determine the threshold powers with and without Auger recombination to be 97 nW and 84 nW respectively, corresponding to an increase of only 1.2. Thus, not only does the small mode volume cavity exhibit a much lower overall lasing threshold, but the lasing threshold is also largely unaffected by Auger recombination.

Figure 5.3(b) plots $\eta = P/P'$ as a function of $V_m$, where $P$ is the absorbed pump power at threshold with $\gamma_a = 1/300$ ps$^{-1}$ and $P'$ is the absorbed pump power at threshold with $\gamma_a = 0$. We set the total quantum dot number in the cavities to $N = 2N_{opt}$ for each value of $V_m$ (Fig. 5.2(b)). From this curve, we observe that below a mode-volume of 0.1 $\mu m^3$ the lasing threshold is largely unaffected by Auger recombination. Above this mode volume, $\eta$ rapidly increases and eventually reaches a saturated value. At large mode-volumes, $\eta$ becomes independent of the mode volume itself and achieves an asymptotic limit. From the upper and the lower limits of $\eta$ (21 and 1.2, respectively), we determine that spontaneous emission enhancement can reduce the lasing threshold up to a factor of 17.

To verify that the improvement in lasing threshold is due to spontaneous emission enhancement, we calculate the spontaneous emission coupling efficiency

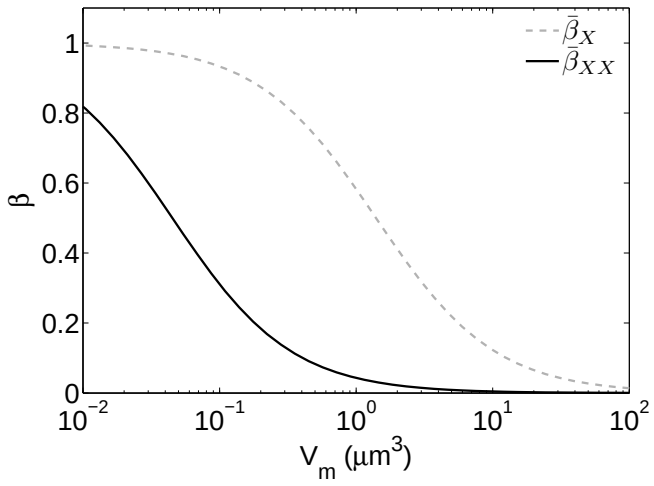


Figure 5.4: Spontaneous emission coupling efficiency for single-exciton transition $\bar{\beta}_X$ and biexciton transition $\bar{\beta}_{XX}$ as a function of $V_m$ for $\gamma_a = 1/300$ ps$^{-1}$

for the exciton and biexciton transition as a function of $V_m$. Using the uniform field approximation, we replace $\Gamma_i(\mathbf{r})$ (i = X, XX) in Eqs. (5.16) - (5.17) with its spatially averaged value $\bar{\Gamma}_i$ which removes the spatial dependence and results in the simplified expressions for the coupling efficiencies given by

$$\bar{\beta}_X = \frac{\bar{\Gamma}_X}{\bar{\Gamma}_X + \gamma_0} \tag{5.28}$$

$$\bar{\beta}_{XX} = \frac{\bar{\Gamma}_{XX}}{\bar{\Gamma}_{XX} + \gamma_2} \tag{5.29}$$

Figure 5.4 plots spontaneous emission coupling efficiencies for the single-exciton transition $\bar{\beta}_X$ and the biexciton transition $\bar{\beta}_{XX}$ as a function of $V_m$ using $\gamma_a = 1/300$ ps$^{-1}$. At $V_m = 100\ \mu m^3$, $\bar{\beta}_{XX}$ is more than an order of magnitude smaller than $\bar{\beta}_X$. As the mode volume decreases the two efficiencies approach unity. The coupling efficiency of the biexciton transition begins to increase sharply and approach unity around the same mode-volume where $\eta$ (Fig. 5.3(b)) begins to saturate to unity. Thus, at small mode-volumes $\bar{\beta}_{XX}$ is insensitive to Auger recombination, and there-

fore the threshold pump power does not significantly change as indicated in Fig. 5.3(b).

## 5.4 Cavity device structure for low-threshold laser

The previous section established the advantage of using small mode-volume cavities to achieve low threshold lasing with nanocrystal quantum dots. A promising device structure for attaining this requirement is the nanobeam photonic crystal cavity. Nanobeam photonic crystal cavities have been previously studied in a variety of material systems, such as silicon [21–23], silicon nitride [24,25], silicon dioxide [26–28], and gallium arsenide [29, 30], and have been theoretically predicted to achieve mode-volumes approaching the diffraction limit [22, 23, 28, 31].

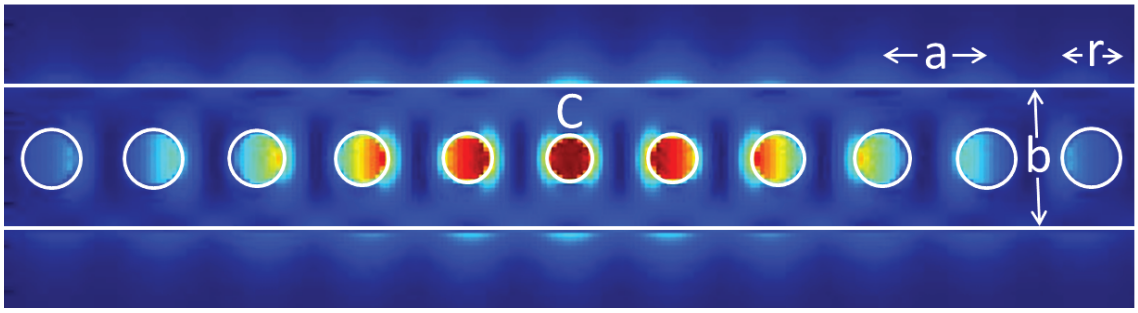


Figure 5.5: The electric field intensity ($|E|^2$) of the resonant cavity mode of a nanobeam photonic crystal cavity. The seven holes in the center form the cavity defect.

Figure 5.5 shows the nanobeam photonic crystal cavity design that we consider for low threshold lasing. Nanocrystal quantum dots are typically spin cast onto the device and therefore reside outside the dielectric. We therefore design the cavity

mode to be localized in the air holes rather than the dielectric material. This design choice maximizes the field overlap with the quantum dots.

The structure is composed of a silicon nitride beam with a one-dimensional periodic array of air holes (radius $r = 0.24a$, where $a$ is the lattice constant). The cavity is composed of a defect in the structure created by gradually reducing the radius of the three holes on either side of the hole labelled C to a minimum of $r_0 = 0.2a$. The adiabatic reduction of hole radius creates a smooth confinement for the photon and minimizes scattering due to edge states [104]. The cavity is designed with beam thickness $d = 0.727a$ and beam width $b = 1.163a$. The index of refraction of silicon nitride is set to 2.01 [72]. We calculate the mode of the cavity using three dimensional finite-difference time-domain simulation (Lumerical Solutions, Inc.). Figure 5.5 shows the calculated electric field intensity overlaid on the structure. The computed mode-volume is $V_m = 0.38\lambda^3$ ($= 0.11\ \mu m^3$) and the quality factor is $Q = 64,000$.

Nanobeam photonic crystal cavities achieve mode-volumes that are on the order of a cubic wavelength. When the confinement volume of the cavity approaches the spatial variation of the field distribution, the uniform-field approximation can break down. We therefore analyze the nanobeam laser both with and without this approximation. We calculate $\epsilon_{eff} = 1.9$ for the cavity by numerically integrating Eq. (5.19) using the computed electric field intensity profile of the simulated cavity structure (Fig. 5.5). Calculations under the uniform-field approximation follow the same approach as in the section 5.3.

In order to investigate the input-output characteristics of the nanobeam laser

without the uniform-field approximation, we first determine the total number of quantum dots required for achieving lasing threshold. We assume a uniform volume-density of quantum dots, denoted by $n = N/V_p$ where $V_p$ is the volume of the optically pumped region. We assume quantum dots reside only in the air holes and on the top of the nanobeam, which are optically pumped with an illumination spot with a diameter of 690 nm, covering the central three holes of the cavity (Fig. 5.5). We divide the illuminated volume into small volume elements (with volume $\Delta V$ at location $\mathbf{r}$) and numerically solve Eqs. (5.7)- (5.10) and Eq. (5.12) in steady state, along with the conditions $\sum_j n_j(\mathbf{r}) = n$ for each volume element, and numerically determine the required $n$ to achieve $\lim_{p\to 0} G(p) = \kappa$. We assume that absorption loss due to quantum dots outside of the excitation volume are negligible compared to other loss mechanisms in the cavity.

Using the same simulation parameters as in the previous section, we numerically calculate the minimum number of quantum dots required to achieve threshold to be $N_{opt} = 60$. This number is nearly identical to the value calculated using the uniform-field approximation which is 62. Next, we calculate the light-in light out curve using Eq. (5.14) and Eq. (5.15) without the uniform-field approximation. As in the previous section, we set the total number of quantum dots to be $N = 2N_{opt}$.

Figure 5.6(a) plots $P_{out}$ as a function of $P_{abs}$ for the nanobeam photonic crystal cavity with simulated $Q = 64,000$ using $\gamma_a = 1/300$ ps$^{-1}$ and 0, both with and without the uniform-field approximation. The calculations show good agreement between the predicted input-output characteristics of the laser with and without the uniform-field approximation. Without the uniform-field approximation, the ab-

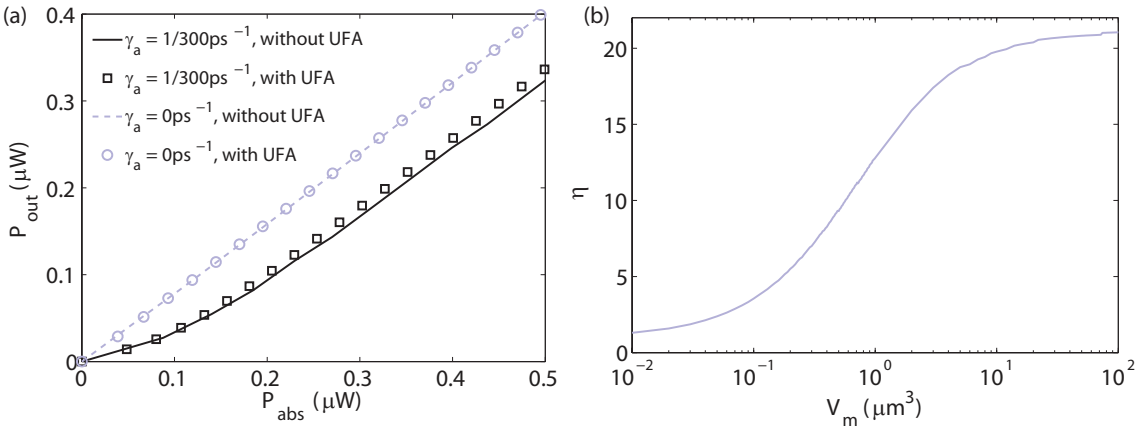


Figure 5.6: (a) Output power as a function of the absorbed pump power for nanocrystal quantum dot laser comprised of nanobeam photonic crystal cavity, using $\gamma_a = 1/300$ ps$^{-1}$ and 0, both with and without uniform-field approximation (abbreviated as UFA in the legend). (b) $\eta$ as a function of mode-volume under the uniform-field approximation for $\epsilon_{eff} = 1.9$ and $Q = 64{,}000$.

sorbed pump power at threshold for the nanobeam laser is 109.8 nW for $\gamma_a = 1/300$ ps$^{-1}$ and 29.9 nW for $\gamma_a = 0$, resulting in $\eta = 3.7$. With the uniform-field approximation, the absorbed pump power at threshold for the nanobeam laser is 112.6 nW for $\gamma_a = 1/300$ ps$^{-1}$ and 30 nW for $\gamma_a = 0$, resulting in $\eta = 3.8$.

The $\epsilon_{eff}$ for the nanobeam cavity, calculated from the cavity-field distribution, is 1.9. This calculated $\epsilon_{eff}$ is higher than the unity assumption in the previous section because in this realistic cavity design a fraction of the cavity field leaks into the dielectric medium (Fig. 5.5). Figure 5.6(b) plots $\eta$ as a function of $V_m$ under the uniform-field approximation for the same parameters used in Fig. 5.6(a). For a cavity with a mode volume of 100 $\mu m^3$, we determine that $\eta = 21.1$. This value is 5.6 times larger than the value for the nanobeam cavity. Thus, the nanobeam

cavity lasing threshold is much less sensitive to Auger recombination.

## 5.5 Conclusion

In conclusion, we have theoretically shown that cavity-enhanced spontaneous emission of the biexciton reduces the effect of Auger recombination, leading to a lower lasing threshold. We developed a numerical model for a laser composed of an ensemble of nanocrystal quantum dots coupled to an optical cavity. The model can be expanded to incorporate more complex behavior of nanocrystal quantum dots, such as blinking, by introducing additional trap states into the quantum dot level structure [105, 106]. This model can also be used to study lasing with other room-temperature emitters such as quantum rods [84, 86], and other types of cavities such as plasmonic apertures [107]. Our results provide a direction for development of low-threshold and highly tunable nanolasers that use nanocrystal quantum dot as gain material at room temperature.

# Chapter 6: Deterministic Deposition of Quantum Dots using Dip-pen Nanolithography

## 6.1 Motivation

To develop nanophotonic devices such as nanolasers, quantum dots need to be localized in the cavity region, so that they do not act as absorbers or scatterers in other parts of the devices. However, the common method of depositing colloidal quantum dots, dab-casting or spin-casting, which we also used in our previous measurements, leads to stochastic deposition of quantum dots on the devices. Figure 6.1 shows AFM images of the nanobeam cavities we used in previous measurements. This stochastic deposition of quantum dots leads to degradation of the cavity quality factors due to the presence of quantum dots in the defect-free region (away from the cavity region) of the nanobeam.

For more controlled deposition of quantum dots on the cavities and better fabrication of quantum dot devices, we are using a dip-pen nanolithigrapy technique [108, 109] which uses an atomic force microscope (AFM) for precise deposition of quantum dots.

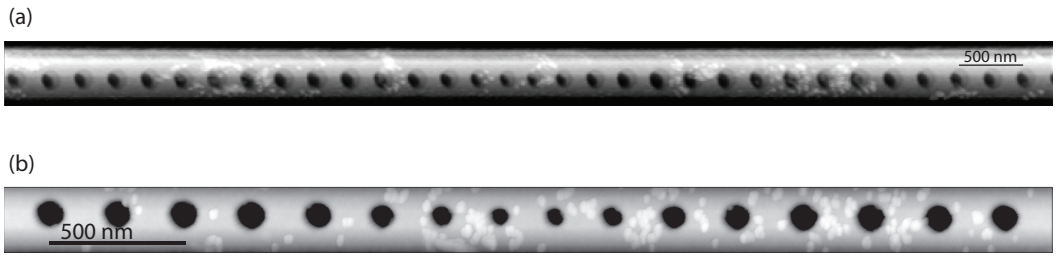


Figure 6.1: (a)AFM image of a nanobeam with low concentration of quantum dots, used for lifetime measurements. (b) AFM image of a nanobeam with high concentration of quantum dots, used for saturable absorption measurements.

## 6.2 Dip-pen Nanolithography

Dip-pen nanolithography is a technique that uses an AFM-tip as a "pen-nib", substrate (SiN here) as "paper", and chemicals to be deposited deterministically (quantum dots here) as "ink" [108]. This technique allows single-step lithography with sub-50-nm resolution and does not involve any pre-modification of the substrate [109]. This technique originated from a problem that affects high-resolution imaging using AFM in ambient conditions: the narrow gap capillary between the AFM tip and the substrate results in condensation of the ambient moisture in the gap, and thus influences imaging [108]. Piner et al. [108] converted this imaging problem into dip-pen nanolithography technique by using the the meniscus to transfer "ink" to the substrate. Many factors affect the transport of the "ink" to the substrate. Higher relative humidity [110], longer dwell time of the tip on the substrate [111] and hydrophillic substrates [112] help in formation of larger meniscus and more transfer of ink molecules.

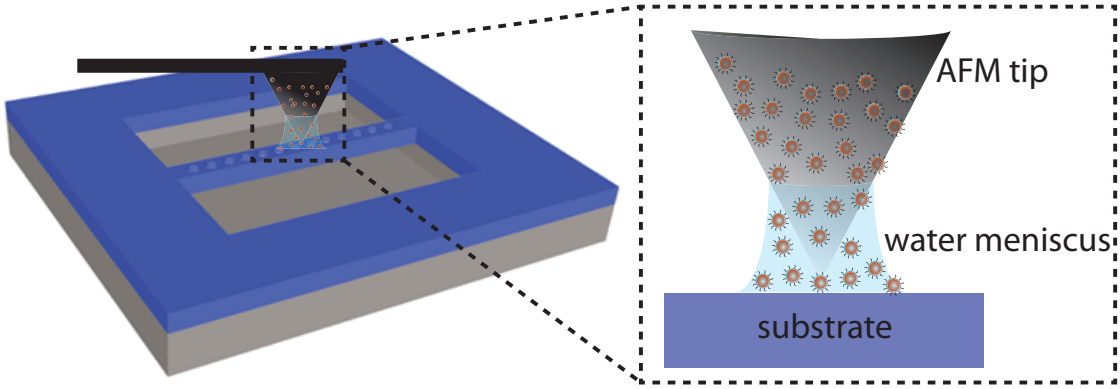


Figure 6.2: Illustration of dip-pen nanolithography technique for depositing colloidal quantum dots on nanobeam photonic crystal cavity. The inset shows formation of water meniscus and transfer of quantum dots when a prepared AFM tip is brought close to a substrate.

Dip-pen nanolithography has been extensively used for patterning organic molecules [108, 113], DNA [114, 115], and proteins [116] for biological applications. For photonics applications, CdSe quantum dots were deposited on a gold surface in the form of patches and lines, and photoluminescence from the deposited quantum dots was shown [117]. In another variant of dip-pen nanolithography, nitrogen vacancy centers [118], gold nanorods and gold spheres [119] were maneuvered using an AFM tip on different locations on photonic crystal cavities. In our work, we are using dip-pen nanolithography to deterministically deposit quantum dots on pre-patterned photonic crystal devices. Figure 6.2 shows an illustration of the deposition technique, with inset showing the formation of water meniscus between the AFM tip and the substrate, and the transport of quantum dots.

## 6.3 Experiment

For dip-pen nanolithography, we prepare a SiN AFM probe (Bruker AFM probes: DNP-10A) by immersing it in a 2$\mu$M aqueous solution of CdSe/ZnS quantum dots (Invitrogen Qtracker CdSe/ZnS 655 nm) for 15 minutes. The photonic crystal cavity design and fabrication are the same as in Chapter 3 and 4. We load the photonic crystal sample in an AFM (Cypher, Asylum Research) over a water pool (15 mm in diameter and 3 mm high) to create a humid environment (humidity greater than 20%). The AFM is maintained at 30 °C. The prepared tip is mounted in droplet holder (Asylum Research) such that the tip, the sample and the water pool remain in an enclosed volume. The entire deposition is done in the enclosed high-humidity volume.

For deposition on the nanobeam cavity, we first scan it in amplitude modulated mode to locate its center. The tip is then moved to the center of the beam and approaches the surface until its deflection increases by a set amount. The probe dwells on the surface before it is retracted to a distance of 500 nm. We repeat it multiple times with different dwell times.

After deposition, we conduct photoluminescence and time-resolved measurements on the nanobeam. The sample is loaded into a sealed chamber filled with purified nitrogen gas to prevent oxidation and photo-bleaching of the quantum dots during the experiment. We follow the same measurement technique as in Chapter 3. Figure 6.3 shows the preliminary data. Figure 6.3(a) shows a camera image of the sample when illuminated by white light and a green laser spot covering the entire

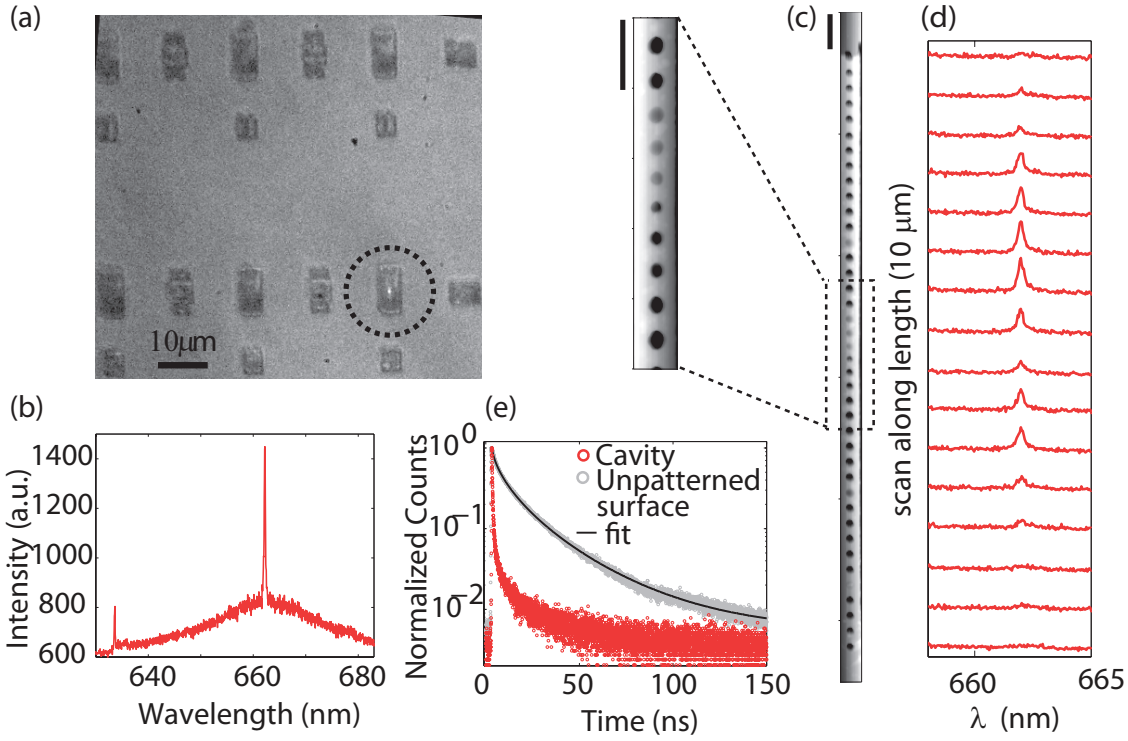


Figure 6.3: (a) Camera image of the sample when illuminated by white light and a green laser spot covering the entire area. The working device (marked by a dashed circle) has a bright spot in the center. (b) Photoluminescence spectrum of the cavity mode. (c) Atomic force microscope image of the device after quantum dot deposition, with inset showing the center of the cavity. The scale bars correspond to 500 nm. (d) Photoluminescence spectra taken along the 10 $\mu$m length of the nanobeam with a UV laser ($\approx$ 1 $\mu$m spot size) in steps of $\approx$ 600 nm. (e) Time-resolved lifetime measurement of quantum dots on the cavity and on the unpatterned surface.

area. The deposited device (marked by a dashed circle) has a bright spot in the center. Figure 6.3(b) shows a photoluminescence spectrum of the cavity mode with $Q = 2500$. Figure 6.3(c) shows an AFM image of the device after quantum dot deposition, taken using a high frequency Si AFM probe (Olympus, AC55TS). The deposited area (shown in the inset) shows a film on top of the holes. In ongoing work, we are investigating how to resolve individual quantum dots deposited using this technique. Figure 6.3(d) shows a scan of photoluminescence spectra across the length of the nanobeam. The measurement was taken using a UV laser spot size of $\approx 1$ $\mu$m and in steps of $\approx 600$ nm. Figure 6.3(e) shows the time-resolved lifetime measurement of the quantum dots deposited on the nanobeam and on unpatterned surface, and the cavity lifetime is much shorter than the quantum dots on the unpatterned surface. In ongoing work, we are conducting more experiments with different types of quantum dots to further develop this technique. We also plan to investigate how surface chemistry and ligands attached to quantum dots affect the deposition.

# Chapter 7: Conclusion and Future Directions

In this thesis, I have demonstrated enhanced interaction between colloidal quantum dots and photonic crystal cavities at room temperature. I achieved an average of 4.6 fold increase in spontaneous emission rate of quantum dots coupled to the cavity. This enhancement can be further improved by embedding the quantum dots in the dielectric, where most of the cavity field is concentrated. Another possible way to improve the enhancement is to use the cavity design suggested in Chapter 5 in which the cavity field is concentrated in the air holes. I also demonstrated saturable absorption of quantum dots coupled to the cavity mode by showing pump-intensity dependent cavity-linewidth. Saturable absorption of these quantum dots is interesting for developing optical switches at room temperature and is a precursor to lasing. With higher spontaneous emission enhancement, low-threshold lasing with colloidal quantum dots can be achieved.

Apart from high photoluminescence efficiency at room temperature, colloidal quantum dots are attractive gain material because their emission wavelength is a function of their physical size and they are not bound to any substrate. Thus, a number of quantum dot devices, like nanolasers and modulators, operating at different frequencies can be accommodated on a single semiconductor chip. This is

important for developing integrated photonic devices which can have applications ranging from optical communication to biological sensing. And our recent work on deterministic placement of colloidal quantum dots on photonic crystal cavities, using dip-pen nanolithography, can be an important step towards this direction, via which different types of quantum dots can be placed on different photonic devices, all located on the same semiconductor chip. The technique needs to be further developed to achieve these goals.

## A.1 Liouvillian superoperator L

The Liouvillian superoperator $\mathbf{L}$ can be expressed as $\mathbf{L} = \mathbf{L_{NQD}} + \mathbf{L_{pump}} + \mathbf{L_{cavity}}$, where $\mathbf{L_{NQD}}$ accounts for the spontaneous relaxation of the quantum dot level structure, $\mathbf{L_{pump}}$ accounts for the incoherent pumping of the quantum dot population, and $\mathbf{L_{cavity}}$ accounts for the cavity decay. These operators are

$$\begin{aligned}
\mathbf{L_{NQD}}\rho = \sum_{m=1}^{N} & \frac{\gamma_{0,m}}{2}(2\sigma_{12,m}\rho\sigma_{21,m} - \sigma_{21,m}\sigma_{12,m}\rho - \rho\sigma_{21,m}\sigma_{12,m} \\
+ & \ 2\sigma_{13,m}\rho\sigma_{31,m} - \sigma_{31,m}\sigma_{13,m}\rho - \rho\sigma_{31,m}\sigma_{13,m}) \\
+ & \frac{\gamma_{2,m}}{2}(2\sigma_{24,m}\rho\sigma_{42,m} - \sigma_{42,m}\sigma_{24,m}\rho - \rho\sigma_{42,m}\sigma_{24,m} \\
+ & \ 2\sigma_{34,m}\rho\sigma_{43,m} - \sigma_{43,m}\sigma_{34,m}\rho - \rho\sigma_{43,m}\sigma_{34,m}) \qquad (1)
\end{aligned}$$

$$\begin{aligned}
\mathbf{L_{pump}}\rho = \sum_{m=1}^{N} & \frac{R}{2}(2\sigma_{21,m}\rho\sigma_{12,m} - \sigma_{12,m}\sigma_{21,m}\rho - \rho\sigma_{12,m}\sigma_{21,m} \\
+ & \ 2\sigma_{31,m}\rho\sigma_{13,m} - \sigma_{13,m}\sigma_{31,m}\rho - \rho\sigma_{13,m}\sigma_{31,m} \\
+ & \ 2\sigma_{42,m}\rho\sigma_{24,m} - \sigma_{24,m}\sigma_{42,m}\rho - \rho\sigma_{24,m}\sigma_{42,m} \\
+ & \ 2\sigma_{43,m}\rho\sigma_{34,m} - \sigma_{34,m}\sigma_{43,m}\rho - \rho\sigma_{34,m}\sigma_{43,m}) \qquad (2)
\end{aligned}$$

$$\mathbf{L_{cavity}}\rho = \frac{\kappa}{2}(2\mathbf{a}\rho\mathbf{a}^{\dagger} - \mathbf{a}^{\dagger}\mathbf{a}\rho - \rho\mathbf{a}^{\dagger}\mathbf{a}) \qquad (3)$$

The cavity energy decay rate is $\kappa = \omega_c/Q$.

## A.2 Equations of motion: projected on quantum dot levels

The equations of motion for the projections of $\rho$ on the levels (ij) of the $m^{th}$ quantum dot and photon states (pp') $\rho^{m}_{ip,jp'} =_m \langle i,p|\rho|j,p'\rangle_m$ (i,j = 1 , 2, 3, 4) and

$(p, p' = 0 \text{ to } \infty)$ are obtained using Eq. (5.3):

$$\begin{aligned}\frac{\partial \rho^m_{1p,1p}}{\partial t} &= ig_m\sqrt{p}(\rho^m_{1p,2p-1} - \rho^m_{2p-1,1p} + \rho^m_{1p,3p-1} - \rho^m_{3p-1,1p}) - 2R\rho^m_{1p,1p} \\ &+ \gamma_0(\rho^m_{2p,2p} + \rho^m_{3p,3p}) + \kappa((p+1)\rho^m_{1p+1,1p+1} - p\rho^m_{1p,1p}) \qquad (4)\end{aligned}$$

$$\begin{aligned}\frac{\partial \rho^m_{2p,2p}}{\partial t} &= ig_m(\sqrt{p+1}(\rho^m_{2p,1p+1} - \rho^m_{1p+1,2p}) + \sqrt{p}(\rho^m_{2p,4p-1} - \rho^m_{4p-1,2p})) \\ &- (\gamma_0 + R)\rho^m_{2p,2p} + R\rho^m_{1p,1p} + \gamma_2\rho^m_{4p,4p} + \kappa((p+1)\rho^m_{2p+1,2p+1} - p\rho^m_{2p,2p}) \qquad (5)\end{aligned}$$

$$\begin{aligned}\frac{\partial \rho^m_{3p,3p}}{\partial t} &= ig_m(\sqrt{p+1}(\rho^m_{3p,1p+1} - \rho^m_{1p+1,3p}) + \sqrt{p}(\rho^m_{3p,4p-1} - \rho^m_{4p-1,3p})) \\ &- (\gamma_0 + R)\rho^m_{3p,3p} + R\rho^m_{1p,1p} + \gamma_2\rho^m_{4p,4p} + \kappa((p+1)\rho^m_{3p+1,3p+1} - p\rho^m_{3p,3p}) \qquad (6)\end{aligned}$$

$$\begin{aligned}\frac{\partial \rho^m_{4p,4p}}{\partial t} &= ig_m\sqrt{p+1}(\rho^m_{4p,2p+1} - \rho^m_{2p+1,4p} + \rho^m_{4p,3p+1} - \rho^m_{3p+1,4p}) - 2\gamma_2\rho^m_{3p,3p} \\ &+ R(\rho^m_{2p,2p} + \rho^m_{3p,3p}) + \kappa((p+1)\rho^m_{3p+1,3p+1} - p\rho^m_{3p,3p}) \qquad (7)\end{aligned}$$

$$\frac{\partial \rho^m_{1p,2p-1}}{\partial t} = ig_m\sqrt{p}(\rho^m_{1p,1p} - \rho^m_{2p-1,2p-1}) - K_X\rho^m_{1p,2p-1} \qquad (8)$$

$$\frac{\partial \rho^m_{2p,4p-1}}{\partial t} = ig_m\sqrt{p}(\rho^m_{2p,2p} - \rho^m_{4p-1,4p-1}) - K_{XX}\rho^m_{2p,4p-1} \qquad (9)$$

$$\frac{\partial \rho^m_{1p,3p-1}}{\partial t} = ig_m\sqrt{p}(\rho^m_{1p,1p} - \rho^m_{3p-1,3p-1}) - K_X\rho^m_{1p,3p-1} \qquad (10)$$

$$\frac{\partial \rho^m_{3p,4p-1}}{\partial t} = ig_m\sqrt{p}(\rho^m_{3p,3p} - \rho^m_{4p-1,4p-1}) - K_{XX}\rho^m_{3p,4p-1} \qquad (11)$$

Here, $K_X = (\gamma_0 + \gamma_d + 3R)/2$ and $K_{XX} = (\gamma_0 + 2\gamma_2 + \gamma_d + R)/2$ are the total relaxation rates of the diagonal terms, and $\gamma_d$ is the dephasing rate of the quantum dot (added phenomenologically). We set dephasing rate to be much greater than the cavity decay rate $\gamma_d \gg \kappa$, allowing us to drop the cavity decay contributions from the equations of motion of off-diagonal terms (Eqs. (8) - (11)). Large dephasing

rate also allows us to adiabatically eliminate the expectation value $\langle \rho_{ip,jp'} \rangle$ of the off-diagonal terms $(i \neq j)$from Eqs. (8) - (11), and reduces Eqs. (4) - (7) to

$$\begin{aligned} \frac{\partial \rho^m_{1p,1p}}{\partial t} &= \frac{2g_m^2}{K_X}(\rho^m_{2p-1,2p-1} + \rho^m_{3p-1,3p-1} - 2\rho^m_{1p,1p})p - 2R\rho^m_{1p,1p} \\ &+ \gamma_0(\rho^m_{2p,2p} + \rho^m_{3p,3p}) + \kappa((p+1)\rho^m_{1p+1,1p+1} - p\rho^m_{1p,1p}) \end{aligned} \tag{12}$$

$$\begin{aligned} \frac{\partial \rho^m_{2p,2p}}{\partial t} &= -\frac{2g_m^2}{K_X}(\rho^m_{2p,2p} - \rho^m_{1p+1,1p+1})(p+1) + \frac{2g_m^2}{K_{XX}}(\rho^m_{4p-1,4p-1} - \rho^m_{2p,2p})p \\ &- (\gamma_0 + R)\rho^m_{2p,2p} + R\rho^m_{1p,1p} + \gamma_2\rho^m_{4p,4p} + \kappa((p+1)\rho^m_{2p+1,2p+1} - p\rho^m_{2p,2p}) \end{aligned} \tag{13}$$

$$\begin{aligned} \frac{\partial \rho^m_{3p,3p}}{\partial t} &= -\frac{2g_m^2}{K_X}(\rho^m_{3p,3p} - \rho^m_{1p+1,1p+1})(p+1) + \frac{2g_m^2}{K_{XX}}(\rho^m_{4p-1,4p-1} - \rho^m_{3p,3p})p \\ &- (\gamma_0 + R)\rho^m_{3p,3p} + R\rho^m_{1p,1p} + \gamma_2\rho^m_{4p,4p} + \kappa((p+1)\rho^m_{3p+1,3p+1} - p\rho^m_{3p,3p}) \end{aligned} \tag{14}$$

$$\begin{aligned} \frac{\partial \rho^m_{4p,4p}}{\partial t} &= -\frac{2g_m^2}{K_{XX}}(2\rho^m_{4p,4p} - \rho^m_{2p+1,2p+1} - \rho^m_{3p+1,3p+1})(p+1) - 2\gamma_2\rho^m_{4p,4p} \\ &+ R(\rho^m_{2p,2p} + \rho^m_{3p,3p}) + \kappa((p+1)\rho^m_{4p+1,4p+1} - p\rho^m_{4p,4p}) \end{aligned} \tag{15}$$

Now, tracing over all the photon states in Eq. (12) - (15), and applying semi-classical approximation to factorize full density matrix element into quantum dot and field parts such that $\rho_{ip,ip} = \rho_{ii}\rho_{pp}$, we get

$$\frac{\partial \rho^m_{11}}{\partial t} = \frac{2g_m^2}{K_X}(\rho^m_{22} + \rho^m_{33} - 2\rho^m_{11})\langle p \rangle + \frac{2g^2}{K_X}(\rho^m_{22} + \rho^m_{33}) - 2R\rho^m_{11} + \gamma_0(\rho^m_{22} + \rho^m_{33}) \tag{16}$$

$$\begin{aligned} \frac{\partial \rho^m_{22}}{\partial t} &= -\frac{2g_m^2}{K_X}(\rho^m_{22} - \rho^m_{11})\langle p \rangle + \frac{2g_m^2}{K_{XX}}(\rho^m_{44} - \rho^m_{22})\langle p \rangle - \frac{2g_m^2}{K_X}\rho^m_{22} + \frac{2g_m^2}{K_{XX}}\rho^m_{44} \\ &- (\gamma_0 + R)\rho^m_{22} + R\rho^m_{11} + \gamma_2\rho^m_{44} \end{aligned} \tag{17}$$

$$\begin{aligned} \frac{\partial \rho^m_{33}}{\partial t} &= -\frac{2g_m^2}{K_X}(\rho^m_{33} - \rho^m_{11})\langle p \rangle + \frac{2g_m^2}{K_{XX}}(\rho^m_{44} - \rho^m_{33})\langle p \rangle - \frac{2g_m^2}{K_X}\rho^m_{33} + \frac{2g_m^2}{K_{XX}}\rho^m_{44} \\ &- (\gamma_0 + R)\rho^m_{33} + R\rho^m_{11} + \gamma_2\rho^m_{44} \end{aligned} \tag{18}$$

$$\frac{\partial \rho_{44}^m}{\partial t} = -\frac{2g_m^2}{K_{XX}}(2\rho_{44}^m - \rho_{22}^m - \rho_{33}^m)\langle p\rangle - \frac{4g_m^2}{K_{XX}}\rho_{44}^m - 2\gamma_2\rho_{44}^m + R(\rho_{22}^m + \rho_{33}^m) \quad (19)$$

where $\langle p\rangle = \sum_p p\rho_{pp}$ is the mean photon number. We define $n_j(\mathbf{r}) = \lim_{\Delta V\to 0}\sum_m \langle\sigma_{jj}^m\rangle/\Delta V$ as the quantum dot population density of the j$^{th}$ lasing level where the sum is carried out over all quantum dots contained in small volume $\Delta V$ at location $\mathbf{r}$ and get Eqs. (5.7) - (5.10).

## A.3 Rate equation for mean cavity photon number

The rate equation for the mean cavity photon number is given by

$$\langle\dot{p}\rangle = \sum_p p\dot{\rho}_{pp} \quad (20)$$

Using Eqs. (12) - (15)

$$\begin{aligned}\langle\dot{p}\rangle = \sum_m\sum_p p \quad \{ & \frac{2g_m^2}{K_X}(\rho_{2p-1,2p-1}^m - \rho_{1p,1p}^m)p - \frac{2g_m^2}{K_X}(\rho_{2p,2p}^m - \rho_{1p+1,1p+1}^m)(p+1) \\ + & \frac{2g_m^2}{K_X}(\rho_{3p-1,3p-1}^m - \rho_{1p,1p}^m)p - \frac{2g_m^2}{K_X}(\rho_{3p,3p}^m - \rho_{1p+1,1p+1}^m)(p+1) \\ + & \frac{2g_m^2}{K_{XX}}(\rho_{4p-1,4p-1}^m - \rho_{2p,2p}^m)p - \frac{2g_m^2}{K_{XX}}(\rho_{4p,4p}^m - \rho_{2p+1,2p+1}^m)(p+1) \\ + & \frac{2g_m^2}{K_{XX}}(\rho_{4p-1,4p-1}^m - \rho_{3p,3p}^m)p - \frac{2g_m^2}{K_{XX}}(\rho_{4p,4p}^m - \rho_{3p+1,3p+1}^m)(p+1) \\ - & \kappa(p\rho_{pp} - (p+1)\rho_{p+1p+1})\} \end{aligned} \quad (21)$$

Applying semi-classical approximation to factorize full density matrix element into quantum dot and field parts $\rho_{ip,ip} = \rho_{ii}\rho_{pp}$, and identifying $\sum_{p=0}^{\infty} p\rho_{p,p} = \langle p\rangle$ gives

$$\begin{aligned}\langle\dot{p}\rangle = & -\kappa\langle p\rangle + \sum_m\{\frac{2g_m^2}{K_X}(\rho_{22}^m + \rho_{33}^m - 2\rho_{11}^m)\langle p\rangle + \frac{2g_m^2}{K_{XX}}(2\rho_{44}^m - \rho_{22}^m - \rho_{33}^m)\langle p\rangle \\ + & \frac{2g_m^2}{K_X}(\rho_{22}^m + \rho_{33}^m) + \frac{4g_m^2}{K_{XX}}\rho_{44}^m\} \end{aligned} \quad (22)$$

Eq. (22) leads us to Eq. (5.11).

## A.4 Expression for $N_j$ under the uniform-field approximation

Assuming total number of quantum dots in the cavity, $N$, such that $\sum_i N_i = N$, Eqs. (5.20)-(5.23) can be solved in the steady-state as

$$N_1 = \left(\frac{(p+1)\bar{\Gamma}_X + \gamma_0}{p\bar{\Gamma}_X + R}\right)\frac{N}{2\zeta} \tag{23}$$

$$N_2 = N_3 = \frac{N}{2\zeta} \tag{24}$$

$$N_4 = \left(\frac{p\bar{\Gamma}_{XX} + R}{(p+1)\bar{\Gamma}_{XX} + \gamma_2}\right)\frac{N}{2\zeta} \tag{25}$$

$$\zeta = \frac{(p+1)\bar{\Gamma}_X + \gamma_0}{2(p\bar{\Gamma}_X + R)} + 1 + \frac{p\bar{\Gamma}_{XX} + R}{2((p+1)\bar{\Gamma}_{XX} + \gamma_2)} \tag{26}$$

where $\zeta$ is the ratio of the total quantum dot population to the total single-exciton quantum dot population.

## A.5 Quantum dot number required for achieving lasing threshold

Under uniform-field approximation

$$N_{th} = \frac{\omega_c}{Q}\left(\frac{\frac{\bar{\Gamma}_X+\gamma_0}{2R} + 1 + \frac{R}{2\bar{\Gamma}_{XX}+2\gamma_2}}{\bar{\Gamma}_X(1 - \frac{\bar{\Gamma}_X+\gamma_0}{R}) + \bar{\Gamma}_{XX}(\frac{R}{\bar{\Gamma}_{XX}+\gamma_2} - 1)}\right) \tag{27}$$

# Bibliography


[1] G. Bjork and Y. Yamamoto. Analysis of semiconductor microcavity lasers using rate equations. *IEEE Journal of Quantum Electronics*, 27(11):2386–2396, 1991.

[2] Hatice Altug, Dirk Englund, and Jelena Vučković. Ultrafast photonic crystal nanocavity laser. *Nature Physics*, 2(7):484–488, July 2006.

[3] Bryan Ellis, Ilya Fushman, Dirk Englund, Bingyang Zhang, Yoshihisa Yamamoto, and Jelena Vučković. Dynamics of quantum dot photonic crystal lasers. *Applied Physics Letters*, 90:151102, 2007.

[4] Kirill A Atlasov, Milan Calic, Karl Fredrik Karlsson, Pascal Gallo, Alok Rudra, Benjamin Dwir, and Eli Kapon. Photonic-crystal microcavity laser with site- controlled quantum-wire active medium. *Optics Express*, 17(20):18178–18183, 2009.

[5] E Fred Schubert and Jong Kyu Kim. Solid-state light sources getting smart. *Science (New York, N.Y.)*, 308(5726):1274–8, May 2005.

[6] Eli Yablonovitch. Inhibited spontaneous emission in solid-state physics and electronics. *Physical review letters*, 58(20):2059–2062, 1987.

[7] M Grätzel. Photoelectrochemical cells. *Nature*, 414(November), 2001.

[8] P Michler, A Kiraz, C Becher, W V Schoenfeld, P M Petroff, L Zhang, E Hu, and A Imamoglu. A quantum dot single-photon turnstile device. *Science (New York, N.Y.)*, 290(5500):2282–5, December 2000.

[9] Dirk Englund, David Fattal, Edo Waks, Glenn Solomon, Bingyang Zhang, Toshihiro Nakaoka, Yasuhiko Arakawa, Yoshihisa Yamamoto, and Jelena Vučković. Controlling the Spontaneous Emission Rate of Single Quantum Dots in a Two-Dimensional Photonic Crystal. *Physical Review Letters*, 95(1):2–5, July 2005.

[10] E. M. Purcell. Spontaneous emission probabilities at radio frequencies. *Physics Review*, 69:681, 1946.

[11] C M Savage and H J Carmichael. Single-Atom Optical Bistability. *IEEE Journal of Quantum Electronics*, 24(8):1495–1498, 1988.

[12] H M Gibbs, S L Mccall, T N C Venkatesan, A C Gossard, A Passner, and W Wiegmann. Optical bistability in semiconductors. *Applied Physics Letters*, 35(6):451–453, 1979.

[13] David A. B. Miller, S. Des Smith, and Colin T. Seaton. Optical Bistability in Semiconductors. *IEEE Journal of Quantum Electronics*, QE-17(3):312–317, 1981.

[14] Christophe Arnold, Vivien Loo, Aristide Lema, Isabelle Sagnes, Olivier Krebs, Paul Voisin, Pascale Senellart, and Loic Lanco. Optical bistability in a quantum dots / micropillar device with a quality factor exceeding 200 000. *Applied Physics Letters*, 100:111111, 2012.

[15] D A B Miller, D S Chemla, D J Eilenberger, P W Smith, A C Gossard, and W T Tsang. Large room temperature optical nonlinearity in GaAs / Ga1 xAlxAs multiple quantum well structures. *Applied Physics Letters*, 41(8):679–681, 1982.

[16] CA Foell, Ellen Schelew, Haijun Qiao, and KA Abel. Saturation behaviour of colloidal PbSe quantum dot exciton emission coupled into silicon photonic circuits. *Optics express*, 20(10):10453–10469, 2012.

[17] Maria Makarova, Vanessa Sih, Joe Warga, Rui Li, Luca Dal Negro, and Jelena Vuckovic. Enhanced light emission in photonic crystal nanocavities with Erbium-doped silicon nanocrystals. *Applied Physics Letters*, 92(16):161107, 2008.

[18] Hitoshi Nakamura. Ultra-fast photonic crystal/quantum dot all-optical switch for future photonic networks. *Lasers and Electro-Optics, ...*, 12(26):6606–6614, 2006.

[19] Akihiko Shinya, Shinji Matsuo, Takasumi Tanabe, Eiichi Kuramochi, Tomonari Sato, Takaaki Kakitsuka, and Masaya Notomi. All-optical on-chip bit memory based on ultra high Q InGaAsP photonic crystal. *Optics Express*, 16(23):19382–19387, 2008.

[20] Deepak Sridharan and Edo Waks. All-Optical Switch Using Quantum-Dot Saturable Absorbers in a DBR Microcavity. *IEEE Journal of Quantum Electronics*, 47(1):31–39, January 2011.

[21] J S Foresi and L C Kimerling. Microcavities in optical waveguides. *Nature*, pages 143–145, 1997.

[22] Parag B. Deotare, Murray W. McCutcheon, Ian W. Frank, Mughees Khan, and Marko Loncar. High quality factor photonic crystal nanobeam cavities. *Applied Physics Letters*, 94(12):121106, 2009.

[23] Qimin Quan and Marko Loncar. Deterministic design of wavelength scale, ultra-high Q photonic crystal nanobeam cavities. *Optics Express*, 19(19):18529–18542, August 2011.

[24] Matt Eichenfield, Ryan Camacho, Jasper Chan, Kerry J Vahala, and Oskar Painter. A picogram- and nanometre-scale photonic-crystal optomechanical cavity. *Nature*, 459(7246):550–5, May 2009.

[25] Mughees Khan, Thomas Babinec, Murray W McCutcheon, Parag Deotare, and Marko Loncar. Fabrication and characterization of high-quality-factor silicon nitride nanobeam cavities. *Optics letters*, 36(3):421–3, February 2011.

[26] P Velha, E Picard, T Charvolin, E Hadji, J C Rodier, P Lalanne, and D Peyrade. Ultra-High Q/V Fabry-Perot microcavity on SOI substrate. *Optics express*, 15(24):16090–6, November 2007.

[27] Ahmad R Zain, Nigel P Johnson, Marc Sorel, and Richard M De La Rue. Ultra high quality factor one dimensional photonic crystal/photonic wire microcavities in silicon-on-insulator (SOI). *Optics express*, 16(16):12084–9, August 2008.

[28] Yiyang Gong and Jelena Vuckovic. Photonic crystal cavities in silicon dioxide. *Applied Physics Letters*, 96(3):031107, 2010.

[29] Armand Rundquist, Arka Majumdar, and Jelena Vuckovic. Off-resonant coupling between a single quantum dot and a nanobeam photonic crystal cavity. *Applied Physics Letters*, 99(25):251907, 2011.

[30] Kelley Rivoire, Sonia Buckley, and Jelena Vuckovic. Multiply resonant high quality photonic crystal nanocavities. *Applied Physics Letters*, 99(1):013114, 2011.

[31] Jasper Chan, Matt Eichenfield, Ryan Camacho, and Oskar Painter. Optical and mechanical design of a zipper photonic crystal optomechanical cavity Abstract :. 17(5):555–560, 2009.

[32] C. B. Murray, D. J. Noms and M. G. Bawendi. Synthesis and Characterization of Nearly Monodisperse CdE (E = S, Se, Te) Semiconductor Nanocrystallites. *J. Am. Chem. Soc*, 115(4):8706–8715, 1993.

[33] A. P. Alivisatos. Semiconductor clusters, nanocrystals, and quantum dots. *Science*, 271:933, 1996.

[34] Victor I Klimov. From fundamental photophysics to multicolor lasing. *Los Alamos Science*, 28:214–220, 2003.

[35] Susumu Noda, Masayuki Fujita, and Takashi Asano. Spontaneous-emission control by photonic crystals and nanocavities. *Nature Photonics*, 1(8):449–458, August 2007.

[36] Marko Lončar, Tomoyuki Yoshie, Axel Scherer, Pawan Gogna, and Yueming Qiu. Low-threshold photonic crystal laser. *Applied Physics Letters*, 81(15):2680–2682, 2002.

[37] D.G. Deppe T. Yoshie, O.B. Shchekin, H. Chen and A. Scherer. Quantum dot photonic crystal lasers. *Electronic Letters*, 38(17):967–968, 2002.

[38] H Y Ryu, M Notomi, E Kuramoti, and T Segawa. Large spontaneous emission factor ( $> 0$ . 1 ) in the photonic crystal monopole-mode laser. *Applied Physics Letters*, 84(7):1067–1069, 2004.

[39] S Strauf, K Hennessy, M T Rakher, Y Choi, A Badolato, L C Andreani, E L Hu, P M Petroff, and D Bouwmeester. Self-Tuned Quantum Dot Gain in Photonic Crystal Lasers. *Physical Review Letters*, 96:127404, 2006.

[40] Susumu Noda. Photonic crystal lasers ultimate nanolasers and broad-area coherent lasers [ Invited ]. *Journal of Optical Society of America B*, 27(11):1–8, 2010.

[41] Marin Soljac, ic, , Mihai Ibanescu, Steven G. Johnson, Yoel Fink, and J. D. Joannopoulos. Optimal bistable switching in nonlinear photonic crystals. *Physical Review E*, 66:055501, 2002.

[42] Xiaodong Yang, Chad Husko, Chee Wei Wong, Mingbin Yu, and Dim-lee Kwong. Observation of femtojoule optical bistability involving Fano resonances in in high-Q/Vm silicon photonic crystal nanocavities Xiaodong. *Applied Physics Letters*, 91:051113, 2007.

[43] Kengo Nozaki, Takasumi Tanabe, Akihiko Shinya, Shinji Matsuo, Tomonari Sato, Hideaki Taniyama, and Masaya Notomi. Sub-femtojoule all-optical switching using a photonic-crystal nanocavity. *Nature Photonics*, 4(7):477–483, May 2010.

[44] Ranojoy Bose, Deepak Sridharan, Hyochul Kim, Glenn S. Solomon, and Edo Waks. Low-Photon-Number Optical Switching with a Single Quantum Dot Coupled to a Photonic Crystal Cavity. *Physical Review Letters*, 108(22):227402, May 2012.

[45] BS Mashford, Matthew Stevenson, and Zoran Popovic. High-efficiency quantum-dot light-emitting devices with enhanced charge injection. *Nature*, (April):2–7, 2013.

[46] Lei Qian, Ying Zheng, Jiangeng Xue, and PH Holloway. Stable and efficient quantum-dot light-emitting diodes based on solution-processed multilayer structures. *Nature photonics*, 5(September), 2011.

[47] P. T. Snee, Y. Chan, D. G. Nocera, and M. G. Bawendi. Whispering-Gallery-Mode Lasing from a Semiconductor Nanocrystal/Microsphere Resonator Composite. *Advanced Materials*, 17(9):1131–1136, May 2005.

[48] Bumki Min, Sungjee Kim, Koichi Okamoto, Lan Yang, Axel Scherer, Harry Atwater, and Kerry Vahala. Ultralow threshold on-chip microcavity nanocrystal quantum dot lasers. *Applied Physics Letters*, 89(19):191124, 2006.

[49] Hans-Jurgen Eisler, Vikram C. Sundar, Moungi G. Bawendi, Michael Walsh, Henry I. Smith, and Victor Klimov. Color-selective semiconductor nanocrystal laser. *Applied Physics Letters*, 80(24):4614, 2002.

[50] J. Lee, V. C. Sundar, J. R. Heine, M. G. Bawendi, and K. F. Jensen. Full Color Emission from IIVI Semiconductor Quantum DotPolymer Composites. *Advanced Materials*, 12(15):1102–1105, 2000.

[51] Lianhua Qu and Xiaogang Peng. Control of photoluminescence properties of CdSe nanocrystals in growth. *Journal of the American Chemical Society*, 124(9):2049–55, March 2002.

[52] JM Gerard. Solid-state cavity-quantum electrodynamics with self-assembled quantum dots. *Single Quantum Dots, Topics Appl. Phys.*, 90:283–327, 2003.

[53] Luigi Martiradonna, Luigi Carbone, Aniwat Tandaechanurat, Masatoshi Kitamura, Satoshi Iwamoto, Liberato Manna, Massimo De Vittorio, Roberto Cingolani, and Yasuhiko Arakawa. Two-dimensional photonic crystal resist membrane nanocavity embedding colloidal dot-in-a-rod nanocrystals. *Nano letters*, 8(1):260–4, January 2008.

[54] Ferruccio Pisanello, Antonio Qualtieri, Tiziana Stomeo, Luigi Martiradonna, Roberto Cingolani, Alberto Bramati, and Massimo De Vittorio. High-Purcell-factor dipolelike modes at visible wavelengths in H1 photonic crystal cavity. *Optics letters*, 35(10):1509–11, May 2010.

[55] A. Qualtieri, F. Pisanello, M. Grande, T. Stomeo, L. Martiradonna, G. Epifani, a. Fiore, a. Passaseo, and M. De Vittorio. Emission control of colloidal nanocrystals embedded in Si3N4 photonic crystal H1 nanocavities. *Microelectronic Engineering*, 87(5-8):1435–1438, May 2010.

[56] F. Pisanello, L. Martiradonna, a. Qualtieri, T. Stomeo, M. Grande, P.P. Pompa, R. Cingolani, a. Bramati, and M. De Vittorio. Silicon nitride PhC nanocavities as versatile platform for visible spectral range devices. *Photonics and Nanostructures - Fundamentals and Applications*, 10(3):319–324, June 2012.

[57] Nikhil Ganesh, Wei Zhang, Patrick C Mathias, Edmond Chow, J a N T Soares, Viktor Malyarchuk, Adam D Smith, and Brian T Cunningham. Enhanced fluorescence emission from quantum dots on a photonic crystal surface. *Nature nanotechnology*, 2(8):515–20, August 2007.

[58] Shobha Shukla, Rajiv Kumar, Alexander Baev, a. S. L. Gomes, and P. N. Prasad. Control of Spontaneous Emission of CdSe Nanorods in a Multirefringent Triangular Lattice Photonic Crystal. *The Journal of Physical Chemistry Letters*, 1(9):1437–1441, May 2010.

[59] Peter Lodahl, a Floris Van Driel, Ivan S Nikolaev, Arie Irman, Karin Overgaag, Daniël Vanmaekelbergh, and Willem L Vos. Controlling the dynamics of spontaneous emission from quantum dots by photonic crystals. *Nature*, 430(7000):654–7, August 2004.

[60] Murray W Mccutcheon and Marko Loncar. Design of a silicon nitride photonic crystal nanocavity with a Quality factor of one million for coupling to a diamond nanocrystal Abstract :. *Optics Express*, 16(23):408–413, 2008.

[61] Anton V Malko, Young-Shin Park, Siddharth Sampat, Christophe Galland, Javier Vela, Yongfen Chen, Jennifer a Hollingsworth, Victor I Klimov, and Han Htoon. Pump-intensity- and shell-thickness-dependent evolution of photoluminescence blinking in individual core/shell CdSe/CdS nanocrystals. *Nano letters*, 11(12):5213–8, December 2011.

[62] Germar Schlegel, Jolanta Bohnenberger, Inga Potapova, and Alf Mews. Fluorescence Decay Time of Single Semiconductor Nanocrystals. *Physical Review Letters*, 88(13):1–4, March 2002.

[63] BR Fisher and HJ Eisler. Emission intensity dependence and single-exponential behavior in single colloidal quantum dot fluorescence lifetimes. *The Journal of Physical Chemistry B*, 108:143–148, 2004.

[64] Ivan Nikolaev, Peter Lodahl, a. van Driel, a. Koenderink, and Willem Vos. Strongly nonexponential time-resolved fluorescence of quantum-dot ensembles in three-dimensional photonic crystals. *Physical Review B*, 75(11):115302, March 2007.

[65] A. van Driel, I. Nikolaev, P. Vergeer, P. Lodahl, D. Vanmaekelbergh, and W. Vos. Statistical analysis of time-resolved emission from ensembles of semiconductor quantum dots: Interpretation of exponential decay models. *Physical Review B*, 75(3):1–8, January 2007.

[66] B Lounis, H. A. Bechtel, D. Gerion, P. Alivisatos, and W. E. Moerner. Photon antibunching in single CdSe/ZnS quantum dot fluorescence. *Chemical Physics Letters*, 329(5-6):399–404, October 2000.

[67] X. Brokmann, L. Coolen, M. Dahan, and J. Hermier. Measurement of the Radiative and Nonradiative Decay Rates of Single CdSe Nanocrystals through a Controlled Modification of their Spontaneous Emission. *Physical Review Letters*, 93(10):107403, September 2004.

[68] X Brokmann, L Coolen, J Hermier, and M Dahan. Emission properties of single CdSe/ZnS quantum dots close to a dielectric interface. *Chemical Physics*, 318(1-2):91–98, November 2005.

[69] S A Crooker, J A Hollingsworth, S Tretiak, and V I Klimov. Spectrally Resolved Dynamics of Energy Transfer in Quantum-Dot Assemblies : Towards Engineered Energy Flows in Artificial Materials S.A. *Physical Review Letters*, 89(18):186802, 2002.

[70] Nathalie de Leon, Brendan Shields, Chun Yu, Dirk Englund, Alexey Akimov, Mikhail Lukin, and Hongkun Park. Tailoring Light-Matter Interaction with a Nanoscale Plasmon Resonator. *Physical Review Letters*, 108(22):1–5, May 2012.

[71] R. Hostein, R. Braive, M. Larque, K.-H. Lee, a. Talneau, L. Le Gratiet, I. Robert-Philip, I. Sagnes, and a. Beveratos. Room temperature spontaneous emission enhancement from quantum dots in photonic crystal slab cavities in the telecommunications C band. *Applied Physics Letters*, 94(12):123101, 2009.

[72] Michael Barth, Josef Kouba, Johannes Stingl, Bernd Löchel, and Oliver Benson. Modification of visible spontaneous emission with silicon nitride photonic crystal nanocavities. *Optics express*, 15(25):17231–40, December 2007.

[73] Wilfried G. J. H. M. van Sark, Patrick L. T. M. Frederix, Dave J. Van den Heuvel, Hans C. Gerritsen, Ageeth a. Bol, Joost N. J. van Lingen, Celso de Mello Donegá, and Andries Meijerink. Photooxidation and Photobleaching of Single CdSe/ZnS Quantum Dots Probed by Room-Temperature Time-Resolved Spectroscopy. *The Journal of Physical Chemistry B*, 105(35):8281–8284, September 2001.

[74] P. T. Guerreiro, S. Ten, N. F. Borrelli, J. Butty, G. E. Jabbour, and N. Peyghambarian. PbS quantum-dot doped glasses as saturable absorbers for mode locking of a Cr:forsterite laser. *Applied Physics Letters*, 71(12):1595, 1997.

[75] Peter W. Milonni and Joseph H. Eberly. *Laser Physics Ch. 5*. Wiley, Hoboken, New Jersey, 2010.

[76] Stefan Stufler, Patrick Ester, Artur Zrenner, and Max Bichler. Power broadening of the exciton linewidth in a single InGaAsGaAs quantum dot. *Applied Physics Letters*, 85(18):4202, 2004.

[77] Martin T Hill. Nanophotonics: lasers go beyond diffraction limit. *Nature nanotechnology*, 4(11):706–7, November 2009.

[78] Shota Kita, Shoji Hachuda, Shota Otsuka, Tatsuro Endo, Yasunori Imai, Yoshiaki Nishijima, Hiroaki Misawa, and Toshihiko Baba. Super-sensitivity in label-free protein sensing using a nanoslot nanolaser. *Optics express*, 19(18):17683–90, August 2011.

[79] Paul L Gourley, Judy K Hendricks, Anthony E McDonald, R Guild Copeland, Keith E Barrett, Cheryl R Gourley, and R K Naviaux. Ultrafast nanolaser flow device for detecting cancer in single cells. *Biomedical microdevices*, 7(4):331–9, December 2005.

[80] Teresa Pellegrino Wolfgang J Parak, Daniele Gerion, Shara CWilliams Daniela Zanchet, Christine Micheel, Carolyn A Larabelland Rosanne Boudreau, Mark A Le Gros, and A Paul Alivisatos. Biological applications of colloidal nanocrystals. *Nanotechnology*, 14:R15–R27, 2003.

[81] V. I. (ed.) Klimov. *Semiconductor and Metal Nanocrystals: Synthesis and Electronic and Optical Properties*. Marcel Dekker, New York, 2003.

[82] V. I. Klimov, A. A. Mikhailovsky, Su Xu, A. Malko, J. A. Hollingsworth, C. A. Leatherdale, H.-J. Eisler, and M. G. Bawendi. Optical Gain and Stimulated Emission in Nanocrystal Quantum Dots. *Science*, 290(5490):314–317, October 2000.

[83] V. I. Klimov, A. A. Mikhailovsky, D. W. McBranch, C. A. Leatherdale, and M. G. Bawendi. Quantization of Multiparticle Auger Rates in Semiconductor Quantum Dots. *Science*, 287(5455):1011–1013, February 2000.

[84] H. Htoon, J. Hollingsworth, R. Dickerson, and V. Klimov. Effect of Zero- to One-Dimensional Transformation on Multiparticle Auger Recombination in Semiconductor Quantum Rods. *Physical Review Letters*, 91(22):1–4, November 2003.

[85] H. Htoon, J. a. Hollingworth, a. V. Malko, R. Dickerson, and V. I. Klimov. Light amplification in semiconductor nanocrystals: Quantum rods versus quantum dots. *Applied Physics Letters*, 82(26):4776, 2003.

[86] M. Kazes, D.Y. Lewis, Y. Ebenstein, T. Mokari, and U. Banin. Lasing from Semiconductor Quantum Rods in a Cylindrical Microcavity. *Advanced Materials*, 14(4):317, February 2002.

[87] Sergei a. Ivanov, Jagjit Nanda, Andrei Piryatinski, Marc Achermann, Laurent P. Balet, Ilia V. Bezel, Polina O. Anikeeva, Sergei Tretiak, and Victor I. Klimov. Light Amplification Using Inverted Core/Shell Nanocrystals: Towards Lasing in the Single-Exciton Regime. *The Journal of Physical Chemistry B*, 108(30):10625–10630, July 2004.

[88] J. Nanda, S. a. Ivanov, H. Htoon, I. Bezel, a. Piryatinski, S. Tretiak, and V. I. Klimov. Absorption cross sections and Auger recombination lifetimes in inverted core-shell nanocrystals: Implications for lasing performance. *Journal of Applied Physics*, 99(3):034309, 2006.

[89] T. D. Harris & L. E. Brus M. Nirmal, B. O. Dabbousi, M. G. Bawendi, J. J. Macklin, J. K. Trautman. Fluorescence intermittency in single cadmium selenide nanocrystals. *Nature*, 383:802–804, 1996.

[90] Marcus Jones, Jovan Nedeljkovic, Randy J. Ellingson, Arthur J. Nozik, and Garry Rumbles. Photoenhancement of Luminescence in Colloidal CdSe Quantum Dot Solutions. *The Journal of Physical Chemistry B*, 107(41):11346–11352, October 2003.

[91] Yinan Zhang, Irfan Bulu, Wai-Ming Tam, Ben Levitt, Jagdish Shah, Tancredi Botto, and Marko Loncar. High-Q/V air-mode photonic crystal cavities at microwave frequencies. *Optics express*, 19(10):9371–7, May 2011.

[92] J.-Michel Caruge, Yinthai Chan, V. Sundar, H. Eisler, and Moungi Bawendi. Transient photoluminescence and simultaneous amplified spontaneous emission from multiexciton states in CdSe quantum dots. *Physical Review B*, 70(8):1–7, August 2004.

[93] Sa Empedocles, Dj Norris, and Mg Bawendi. Photoluminescence Spectroscopy of Single CdSe Nanocrystallite Quantum Dots. *Physical review letters*, 77(18):3873–3876, October 1996.

[94] S. A. Empedocles and M. G. Bawendi. Influence of Spectral Diffusion on the Line Shapes of Single CdSe Nanocrystallite Quantum Dots. *The Journal of Physical Chemistry B*, 103(11):1826–1830, March 1999.

[95] Dj Norris and Mg Bawendi. Measurement and assignment of the size-dependent optical spectrum in CdSe quantum dots. *Physical review. B, Condensed matter*, 53(24):16338–16346, June 1996.

[96] Daniel. F. Walls and Gerard. J. Milburn. *Quantum Optics*. Springer, 2007.

[97] Oliver Benson and Yoshihisa Yamamoto. Master-equation model of a single-quantum-dot microsphere laser. *Physical Review A*, 59(6):4756–4763, June 1999.

[98] Marcel Bruchez, Mario Moronne, Peter Gin, Shimon Weiss, and A. Paul Alivisatos. Semiconductor nanocrystals as fluorescent biological labels. *Science*, 281(5385):2013–2016, 1998.

[99] Ranojoy Bose, Xiaodong Yang, Rohit Chatterjee, Jie Gao, and Chee Wei Wong. Weak coupling interactions of colloidal lead sulphide nanocrystals with silicon photonic crystal nanocavities near 1.55$\mu$m at room temperature. *Applied Physics Letters*, 90(11):111117, 2007.

[100] Ilya Fushman, Dirk Englund, and Jelena Vuckovic. Coupling of PbS quantum dots to photonic crystal cavities at room temperature. *Applied Physics Letters*, 87(24):241102, 2005.

[101] MT Rakher, Ranojoy Bose, CW Wong, and K Srinivasan. Fiber-based cryogenic and time-resolved spectroscopy of PbS quantum dots. *Optics Express*, 19(3):1786, 2011.

[102] M. T. Rakher, R. Bose, C. W. Wong, and K. Srinivasan. Spectroscopy of 1.55$\mu$m PbS quantum dots on Si photonic crystal cavities with a fiber taper waveguide. *Applied Physics Letters*, 96(16):161108, 2010.

[103] Z. Wu, Z. Mi, P. Bhattacharya, T. Zhu, and J. Xu. Enhanced spontaneous emission at 1.55$\mu$m from colloidal PbSe quantum dots in a Si photonic crystal microcavity. *Applied Physics Letters*, 90(17):171105, 2007.

[104] Qimin Quan, Parag B. Deotare, and Marko Loncar. Photonic crystal nanobeam cavity strongly coupled to the feeding waveguide. *Applied Physics Letters*, 96(20):203102, 2010.

[105] Jing Zhao, Gautham Nair, Brent R. Fisher, and Moungi G. Bawendi. Challenge to the Charging Model of Semiconductor-Nanocrystal Fluorescence Intermittency from Off-State Quantum Yields and Multiexciton Blinking. *Physical Review Letters*, 104(15):1–4, April 2010.

[106] M. Kuno, D. Fromm, S. Johnson, a. Gallagher, and D. Nesbitt. Modeling distributed kinetics in isolated semiconductor quantum dots. *Physical Review B*, 67(12):1–15, March 2003.

[107] Jennifer T. Choy, Birgit J. M. Hausmann, Thomas M. Babinec, Irfan Bulu, Mughees Khan, Patrick Maletinsky, Amir Yacoby, and Marko Lončar. Enhanced single-photon emission from a diamondsilver aperture. *Nature Photonics*, 5(12):738–743, October 2011.

[108] Chad A. Mirkin Richard D. Piner, Jin Zhu, Feng Xu, Seunghun Hong. "Dip-Pen" Nanolithography. *Science*, 283(5402):661–663, January 1999.

[109] Khalid Salaita, Yuhuang Wang, and Chad a Mirkin. Applications of dip-pen nanolithography. *Nature nanotechnology*, 2(3):145–55, March 2007.

[110] Brandon L Weeks, Mark W Vaughn, and James J Deyoreo. Direct imaging of meniscus formation in atomic force microscopy using environmental scanning electron microscopy. *Langmuir : the ACS journal of surfaces and colloids*, 21(18):8096–8, August 2005.

[111] Brandon L Weeks and James J DeYoreo. Dynamic meniscus growth at a scanning probe tip in contact with a gold substrate. *The journal of physical chemistry. B*, 110(21):10231–3, June 2006.

[112] Jennifer R Hampton, Arrelaine a Dameron, and Paul S Weiss. Double-ink dip-pen nanolithography studies elucidate molecular transport. *Journal of the American Chemical Society*, 128(5):1648–53, February 2006.

[113] S. Hong. Multiple Ink Nanolithography: Toward a Multiple-Pen Nano-Plotter. *Science*, 286(5439):523–525, October 1999.

[114] L M Demers, D S Ginger, S-J Park, Z Li, S-W Chung, and C a Mirkin. Direct patterning of modified oligonucleotides on metals and insulators by dip-pen nanolithography. *Science (New York, N.Y.)*, 296(5574):1836–8, June 2002.

[115] Sung-Wook Chung, David S Ginger, Mark W Morales, Zhengfan Zhang, Venkat Chandrasekhar, Mark a Ratner, and Chad a Mirkin. Top-down meets bottom-up: dip-pen nanolithography and DNA-directed assembly of nanoscale electrical circuits. *Small (Weinheim an der Bergstrasse, Germany)*, 1(1):64–9, January 2005.

[116] Ki-Bum Lee, So-Jung Park, Chad a Mirkin, Jennifer C Smith, and Milan Mrksich. Protein nanoarrays generated by dip-pen nanolithography. *Science (New York, N.Y.)*, 295(5560):1702–5, March 2002.

[117] Debdulal Roy, Martin Munz, Paolo Colombi, Sanjib Bhattacharyya, Jean-Paul Salvetat, P.J. Cumpson, and Marie-Louise Saboungi. Directly writing with nanoparticles at the nanoscale using dip-pen nanolithography. *Applied Surface Science*, 254(5):1394–1398, December 2007.

[118] Michael Barth, Nils Nüsse, Bernd Löchel, and Oliver Benson. Controlled coupling of a single-diamond nanocrystal to a photonic crystal cavity. *Optics letters*, 34(7):1108–10, April 2009.

[119] Michael Barth, Stefan Schietinger, Sabine Fischer, Jan Becker, Nils Nüsse, Thomas Aichele, Bernd Löchel, Carsten Sönnichsen, and Oliver Benson. Nanoassembled plasmonic-photonic hybrid cavity for tailored light-matter coupling. *Nano letters*, 10(3):891–5, March 2010.

# Publications

**Journals**

1. Shilpi Gupta and Edo Waks, Overcoming Auger recombination in nanocrystal quantum dot laser using spontaneous emission enhancement, Optics Express, **22**: 3013-3027, 2014 (arXiv:1401.3435 [cond-mat.mes-hall]).

2. Shilpi Gupta and Edo Waks, Spontaneous emission enhancement and saturable absorption of colloidal quantum dots coupled to photonic crystal cavity, Optics Express, **21**: 29612-29619, 2013.

3. Kang-mook Lim, Shilpi Gupta, Chad Ropp and Edo Waks, Development of metal etch mask by single layer lift-off for silicon nitride photonic crystals, Microelectronic Engineering, **88**: 994-998, 2011.

**Conferences**

1. Shilpi Gupta and Edo Waks, Efficient lasing with nanocrystal quantum dots using Purcell effect to overcome Auger recombination, Proceedings of Conference on Lasers and Electro-Optics (CLEO), San Jose, USA, 2012.

2. Shilpi Gupta and Edo Waks, Overcoming Auger recombination in nanocrystal quantum dots using Purcell enhancement, Proceedings of the International Semiconductor Device Research Symposium (ISDRS), College Park, USA, 2011.